STUDIES OF STRATOCUMULUS CLOUD, DRIZZLE AND AEROSOL INTERACTION

by Aidong Chen

Sonia M. Kreidenweis and
David A. Randall, Principal Investigators

Colorado State University

DEPARTMENT OF ATMOSPHERIC SCIENCE

PAPER NO. 603

STUDIES OF STRATOCUMULUS CLOUD, DRIZZLE AND AEROSOL INTERACTION

by

Aidong Chen

Research supported by the
National Science Foundation
under grant number ATM-9215951,
by the National Aeronautics and Space Administration
under grant number NAG1-1137,
and by the Office of Naval Research
under contract number N00014-91-J-1422, P0006

Department of Atmospheric Science
Colorado State University
Fort Collins, CO

April 1996

Atmospheric Science Paper No. 603

Abstract

Studies of Stratocumulus Cloud, Drizzle and Aerosol Interaction

A stratocumulus-capped marine mixed layer model has been developed. It focuses on a new parameterization of drizzle which is regulated by a predicted CCN number concentration.

When the CCN number concentration increases, the drizzle rate decreases, so that the boundary-layer cloud remains thick. When the CCN number concentration decreases, the drizzle rate increases and as a result, the boundary-layer cloud becomes thinner. The boundary layer's macroscopic structure is thus sensitive to the CCN number concentration.

Aerosol particles in this model are divided into two modes. One represents the small nucleation mode particles, and the other represents the CCN mode particles. Both number and mass balances are considered in this report. Two steady states are obtained, similar to the results of Baker and Charlson (1990). The lower steady state CCN number concentration corresponds to the typical marine time boundary layer. The higher steady state CCN number concentration is regarded as the continental air mass case. A difference between the results from this model and those reported by Baker and Charlson (1990) is that a smoother transition between these two states is found. This result supports some observations that suggest there is no sharp transition between the drizzling and non-drizzling steady states of CCN number concentration in the marine boundary layer.

The model is tested using ASTEX observational data. The model results are in good agreement with the observations.

Acknowledgments

I would like to thank my advisors, Drs. Sonia Kreidenweis and David A. Randall, for their great instruction, assistance and encouragement during these past two and a half years. Working with them was a valuable experience and also a great pleasure to me. Thanks to professors Wayne H. Schubert and David Dandy for their helpful ideas and suggestions in preparing and finishing this report.

Thanks also go to Drs. Laura D. Fowler, Ping Ding, and A. Scott Denning for their patience in solving my puzzles. I am grateful to Ross Heikes for his tremendous help with Mathematica. Thanks to Yiping Zhang, Dr. Graham Feingold, Ching-Hsuan Chen and Jerry Harrington for their helpful discussions and suggestions on my research work and to Kelley Ann Wittmeyer for her assistance with using computer facilities. I would also like to thank Cindy Carrick for consulting on FrameMaker and so many other things that I am not able to mention in details. Thanks to Sandy Progen and Haley Brooks for their help with travelling arrangements.

Especially, I would like to thank my husband, Zheng Liu. His love, his understanding and his constant inspiration has been very important through the years.

This research was supported by the National Science Foundation under grant No. ATM-9215951, by the National Aeronautics and Space Administration under grant No. NAG1-1137, and by the Office of Naval Research under contract No. N00014-91-J-1422, P00006.

Table of Contents

Chapter 1

Introduction

1.1. Significance of stratocumulus clouds on climate

Cloud effects have been an important topic in studies of global climate change. Stratocumulus clouds, as many observations have shown, are often persistent and widely spread over large areas of the eastern parts of the subtropical ocean (Schmetz et al., 1983) and arctic regions (Curry and Herman, 1985). These clouds are low warm clouds and usually form at the top of the marine boundary layer (MBL). Satellite imagery has shown that marine stratocumulus clouds reflect more sunlight than the darker ocean surface underneath and reduce the shortwave radiation reaching the earth's surface (Albrecht at al., 1988; Betts and Boers, 1990), since their albedo (30-40%) is much higher than the ocean surface (<10%). Since oceans cover two-thirds of the earth's surface, this effect should be significant. The study of the development and break- up processes of the marine stratiform clouds may help us to understand the role of stratocumulus cloud in the global energy budget. Observational data analysis indicates that low clouds are the largest contributors to the net cloud forcing, about -16 W m^{-2} or 60% of the total net cloud forcing based on a global annually average (Hartmann et al. 1992). A recent seasonal cycle study even showed that mid-latitude summertime stratus clouds might reduce the net radiation budget by 100 W m^{-2} (Klein and Hartmann, 1993). This cooling effect of low clouds has been estimated by Randall et al. (1984) to be such that a 4% increase of marine stratus clouds might offset the predicted 2-3 K warming effect due to a doubling of CO_2.

1.2. Aerosol Effects on Climate

The impact of low stratus clouds on the climate has been widely noticed. However, what factors cause these low clouds to form and last? The study of aerosol chemistry and physics is currently a major topic in climate issues, particularly in understanding the source of cloud condensation nuclei (CCN).

Aerosols may directly affect the Earth's radiation budget by changing the clear sky reflectivity (Charlson, 1991) through their optical properties. They may also indirectly affect the global radiation budget by their impact on the cloud albedo (Twomey, 1977). Aerosols may also affect the hydrological cycle by changing the frequency of cloud formation, cloud thickness and cloud droplet sizes (Albrecht, 1989). Aerosols, either natural or man-made, are the source of cloud condensation nuclei (CCN). An increase in aerosol concentration may increase the number of CCN. It may also enhance the cloud albedo (Twomey et al., 1984). Also, as Albrecht (1989) pointed out, increases in aerosol concentrations may cause decreases in cloud droplet size, and thus reduce the drizzle rate. As a result, the amount of low cloud might tend to increase, which would contribute to a cooling effect on the global climate. On the other hand, since drizzle is an important removal mechanism for aerosol and CCN particles, it has been suggested that at low CCN and droplet concentrations for which drizzle is generally more efficient, the cloud layer may become so thin that cloud-top radiative cooling is not able to drive vertical mixing (Ackerman et al., 1993). The surface moisture supply will be reduced and the lifetime of stratocumulus clouds will be limited.

1.3. Previous Work on MBL Cloud Modeling

MBL stratocumulus-capped models, in the past thirty years, include the earliest simple mixed layer model (Lilly, 1968), one dimensional higher-order closure models (Oliver et al., 1978; Moeng and Randall, 1984), two dimensional higher-order closure models (Moeng and Arakawa, 1980) and three dimensional large-eddy-simulation (LES) models (Deardorff, 1980; Moeng, 1986).

The main advantages of the mixed layer model are its simplicity and computational economy. It works well for a convectively unstable cloud layer with little or no wind shear. For a pure shear-driven boundary layer, the boundary layer is either neutral or stably stratified. Therefore, the well-mixed assumption does not apply. Also, the entrainment assumption is a major uncertainty in the mixed layer model. Although a mixed-layer model can not capture the detailed turbulent structure, it can represent the boundary layer mean structure fairly well.

Higher-order closure models are more general and can simulate more details of turbulent structure. They have fewer limitations and can be applied to various atmospheric conditions. However, their results depend strongly on their closure assumptions, and they cost more in computer time.

LES is a very fundamental approach to modeling the boundary layer's turbulent structure and has become very popular in recent decades. LES models can simulate many details of turbulence and apply to most of the unstable atmospheric states. However, they are very computationally time-consuming, and thus they are generally used to study turbu-

lence only in a limited domain and for a short simulated time interval.

It is conceptually more difficult to represent a physical process in a simple model than in a complicated model. Incorporating a more realistic process in a simple model is a good test of our understanding of the nature of a physical process. Therefore, simple models will always be very important.

The primary issues studied with stratocumulus-capped MBL models are cloud development and breakup processes such as cloud-top entrainment instability (CTEI) (Lilly, 1968; Randall, 1980a; Deardorff, 1980), cloud-top radiative cooling (Lilly and Schubert, 1980), and drizzle effects (Chen and Cotton, 1987). Among these, the drizzle effect has become a focus for recent studies. Scientists used to think of stratiform clouds as non-precipitating clouds. However, in the past decade, many observations show that light precipitation (which is called drizzle) often occurs in these clouds (Brost et al., 1982 and Nicholls, 1984). Some researchers suggested that drizzle may play an important role in regulating the structure of the marine boundary layer (Brost et al., 1982). Albrecht (1989, 1993) used a two-layer boundary layer model to show the effects of drizzle in lowering the boundary layer top height and reducing the cloud fraction.

Chen and Cotton (1987) used a higher-order turbulence closure model to simulate the observed stratocumulus boundary layer under shear-driven turbulence and in the presence of drizzle. The case of buoyancy-driven boundary layer did not apply in their model. Recently, Wang and Wang (1994) presented a high-order turbulence closure model similar to Bougeault (1981), but with a different drizzle parameterization. Their model was able to simulate the details of the turbulence structure and they showed the decoupling effect of

drizzle on boundary layer cloud.

Limited by the high computational costs of LES, it is only recently that LES models have been coupled to cloud microphysical models (Feingold et al., 1994; Stevens et al., 1995). Feingold et al (in press) provided a study on the relationship between turbulent kinetic energy and the drizzle production using the LES version of the Colorado State University Regional Atmospheric Modeling System (RAMS) model, but still in a two dimensional form. Powerful computers will make the three dimensional LES model more feasible for simulation of cloud microphysics in the future.

1.4. Purpose of our study

The objective of this report is to develope a simple stratocumulus-capped well-mixed layer model which includes:

- Boundary layer cloud formation and dissipation processes with drizzle formation which will be regulated by CCN.

- Parameterization of CCN sources, sinks and transports.

A stratocumulus-capped mixed layer model will be explained in detail. A new parameterization involving the interaction of CCN concentrations and drizzle production will be introduced. CCN concentration will be represented by parameterizing the sources, sinks and transports of it within the MBL.

During the 1992 Atlantic Stratocumulus Transition Experiment(ASTEX), boundary layer development and drizzle were observed. A case study from ASTEX will be used

to test the model. The model will also provide a framework for including a drizzling BL into general circulation models in the future.

In this report, the details of the physics in a well-mixed layer will be provided in Chapter 2. The model will be described in Chapter 3. Aerosol and CCN budgets will be presented in Chapter 4. The model's performance will be evaluated in Chapter 5. Chapter 6 presents the conclusions and suggests possibilities for future work.

Chapter 2

The Stratocumulus-Cloud Capped Well-Mixed Layer

2.1. Basic Concepts in a Mixed-layer Model

As mentioned above, the idea of the cloud-capped mixed layer model first came from Lilly's work early in 1968. His theoretical model was a good start in understanding the huge patches of nearly steady marine stratocumulus clouds often observed over the oceans.

As Lilly pointed out, under conditions of strong or moderate large-scale subsidence, the potential temperature of the lower troposphere may be higher than that of the ocean surface. Since the ocean has a tremendous heat capacity, it is nearly impossible to modify the sea surface temperature to match the air temperature. For this reason, there should be an inversion or stable layer near the sea surface. Observations show that this height (z_B) is about 500-1000 meters above the sea surface. This is the definition of the marine boundary layer (MBL) top. Also the turbulent mixing below the inversion may create a fully mixed layer. Neglecting condensation, thermodynamical variables such as the dry static energy ($S = c_pT + gz$) and the water vapor mixing ratio (q) are approximately conserved and so are constant with height in the absence of cloud through the whole MBL.

When water changes phase, the moist static energy ($h = c_pT + gz + Lq_v$) is the conservative variable. If the liquid water (l) does not precipitate, the sum of liquid water

and water vapor mixing ratio ($r_m = q_l + q_v$) will be assumed constant within the MBL.

The typical soundings of these thermodynamics variables over the ocean are shown in Fig. 2.1 (Stull, 1988):

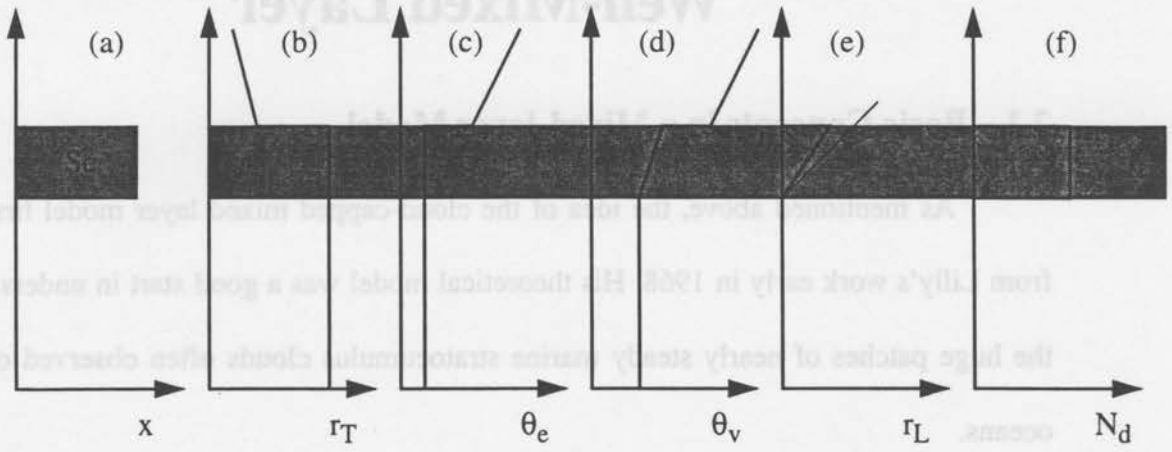

Fig. 2.1. (After Stull 1988, page 570) Idealized profiles of mean variables within a stratocumulus-topped mixed layer. (a) cloud layer location; (b) total water mixing ratio; (c) equivalent potential temperature; (d) virtual potential temperature; (e) liquid water content (thin line indicates the theoretical adiabatic value); (f) number density of cloud droplets.

Fig. 2.1 shows an ideal case of the vertical profiles including the sharp discontinuity at the inversion layer. Total water mixing ratio and equivalent potential temperature are constant with height through the whole layer. Virtual potential temperature follows the moist adiabat within the cloud. Liquid water inside of cloud almost linearly increases with height while at the cloud top it sharply decreases to zero. Cloud droplet number concentration is nearly constant in cloud which indicates that cloud droplet radius is larger at the cloud top. In real soundings, it may be very difficult to identify the MBL top and the values of jumps, which are the differences in variable values between just above the MBL top and just in the MBL.

2.2. Physical Processes

2.2.1 Radiative Cooling and Warming at the Cloud Top

2.2.1.a Longwave Radiative Cooling

Radiative cooling at the cloud top is due to the different radiative properties of water vapor and liquid water droplets. In the infrared spectrum, there is an atmospheric window region between 800 and 1200 cm^{-1} (about 8.3 μm --12.5 μm). Water vapor neither absorbs nor emits in this range. However, liquid water is able to absorb and emit radiation at all infrared wavelengths. Thus, the downward radiation flux emitted by the water vapor just above the cloud top, where the air is dry, is smaller than the upward radiation flux emitted by the liquid water within the cloud. The schematic diagram (Fig. 2.2 (b)) shows that below the cloud top, the upward radiation is nearly uniform. Since the low cloud's temperature is close to the sea surface temperature, the long wave radiation from the cloud is approximately equal to the blackbody emission from the sea surface. The small flux discontinuity at the cloud base reflects the slight temperature difference between the cloud and the sea surface.

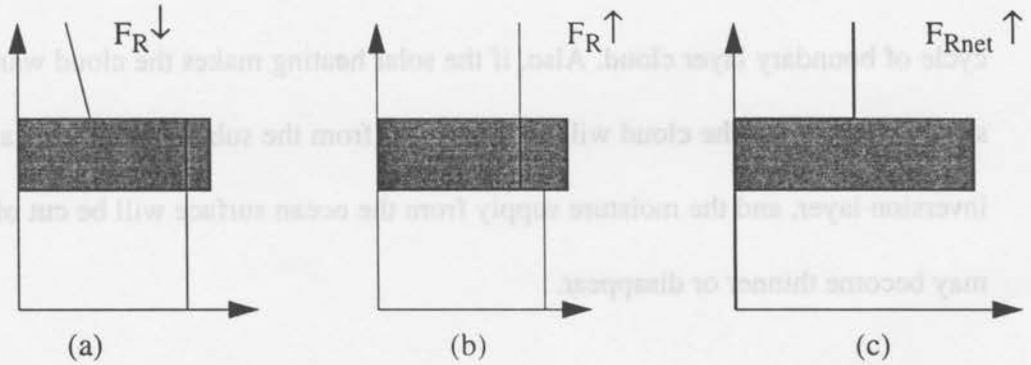

Fig. 2.2. The schematic diagram of longwave radiation flux. (a) the downward radiation flux. (b) the upward radiation flux. (c) the net radiation flux.

As discussed above, there is a net radiative cooling at the cloud top. Lilly (1968) assumed that the radiative cooling is confined to a infinitely thin layer at the cloud top. In his model, a discontinuity of the radiation flux is assumed to occur at the cloud top. This is expressed mathematically as a flux jump condition, ΔR. Later, Kahn and Businger (1979) modified this assumption by using a partially distributed cooling rate within the upper part of the cloud layer. However, As Randall(1980b) pointed out, the location of radiative cooling does not affect the total turbulence. In this model, therefore, the cloud-top flux jump radiation condition is chosen.

When the air just above the cloud top is radiatively cooled, the air parcels being carried below cloud top by the downdrafts are colder than the ambient air. They are negatively buoyant and are accelerated downward (e.g. Shao, 1994). This drives the turbulence.

2.2.1.b Solar Radiative Warming

During daytime, the cloud layer's liquid water absorbs shortwave radiation. As a result, the cloud will be heated and will tend to become thinner. This results in a diurnal cycle of boundary layer cloud. Also, if the solar heating makes the cloud warmer than the subcloud layer air, the cloud will be decoupled from the subcloud layer by a temperature inversion layer, and the moisture supply from the ocean surface will be cut off. The cloud may become thinner or disappear.

In this model, solar radiative warming is not included. The case study to be presented is a nocturnal boundary layer situation.

2.2.2 Entrainment at the Cloud Top

Entrainment happens at the interface of the mixed layer and the stable free atmosphere above the MBL. Turbulent updrafts penetrate through the top of the mixed layer and engulf warm and dry air and carry it back down into the mixed layer. This entrainment of warm air into the less warm mixed layer air contributes to a warming. At the same time, the entrained air is also dry and the cloud droplets inside the mixed layer will evaporate and absorb heat. This is a cooling effect. When the air entrained is warmer and less dry, the warming effect will dominant. The air parcel is warmer than the ambient air. It will stay stable. The mixed layer is less turbulent and entrainment will be decreased. When the air entrained is cooler and more dry, the cooling effect will dominate. As with the radiative cooling discussed in the previous section, the air parcel will become negatively buoyant and sink deeper into the cloud (Fig. 2.3). This may increase turbulence and further enhance the entrainment rate. This is a positive feedback, called cloud-top entrainment instability (CTEI). It is a cloud breakup mechanism first pointed out by Lilly (1968) and modified by Randall (1980a) and Deardorff (1980). A criterion for CTEI is

$$\Delta\theta_e < b/a\ \Delta q_T,$$

where $\Delta\theta_e$ is the jump condition of equivalent potential temperature at the cloud top. b and a are positive thermodynamic coefficients. Δq_T is the jump of total water mixing ratio at the cloud top. When $b=0.$, we get $\Delta\theta_e<0$. This is Lilly's criterion. However, many observations show that even if this condition is satisfied, the stratocumulus cloud still does not break up. Later, Kuo and Schubert (1988) tested and discussed the deficiency of the above condition and pointed out: "Other physical processes (such as surface evaporation) can

apparently moisten the boundary layer rapidly enough to mask the cloud breakup process."

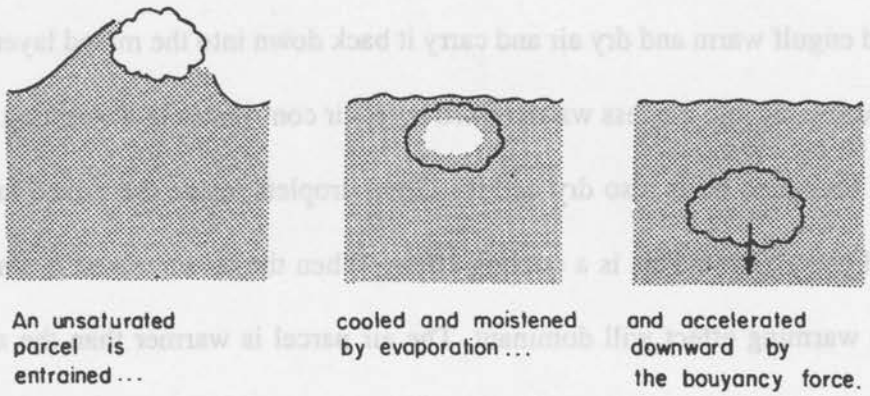

Fig. 2.3. A schematic interpretation of the cloud-top entrainment instability (CTEI). The stippled area represents cloudy air (scanned from Randall, 1980a).

In well-mixed layer modeling, the parameterization of entrainment rate still is a sensitive and uncertain part. Chapter 3 will discuss the details of the parameterization used here. Whether the entrainment is a cloud breakup mechanism or a cloud deepening process (Randall, 1984b) is a very complicated issue which is not focused on in this study.

2.2.3 Drizzle Effect

Although it is a very important physical process in the cloud-topped boundary layer, drizzle has been incorporated into models only within the past ten years. Drizzle depletes liquid water and aerosol particles from the boundary layer. It may modify the total water mixing ratio and further influence the MBL's dynamics. While drizzle falls out of the cloud layer, droplets evaporate in the subcloud layer and cool the ambient air. This may make the subcloud layer cooler than the cloud layer. As with the radiative warming

effect discussed earlier, the cloud layer may become separated from the subcloud layer due to an inversion near the cloud base. The moisture supply from the surface will be cut off by the inversion as well. As a result, the cloud will become thinner.

From an aerosol physics perspective, drizzle is an important removal mechanism. It regulates the aerosol and CCN budget by depleting them from the boundary layer. This will feed back to the boundary layer cloud dissipation process. Drizzle plays a significant role in the discussion of stratocumulus cloud lifetime, and will be analyzed further in the next chapter.

Chapter 3

Model Description

3.1. Basic Assumptions

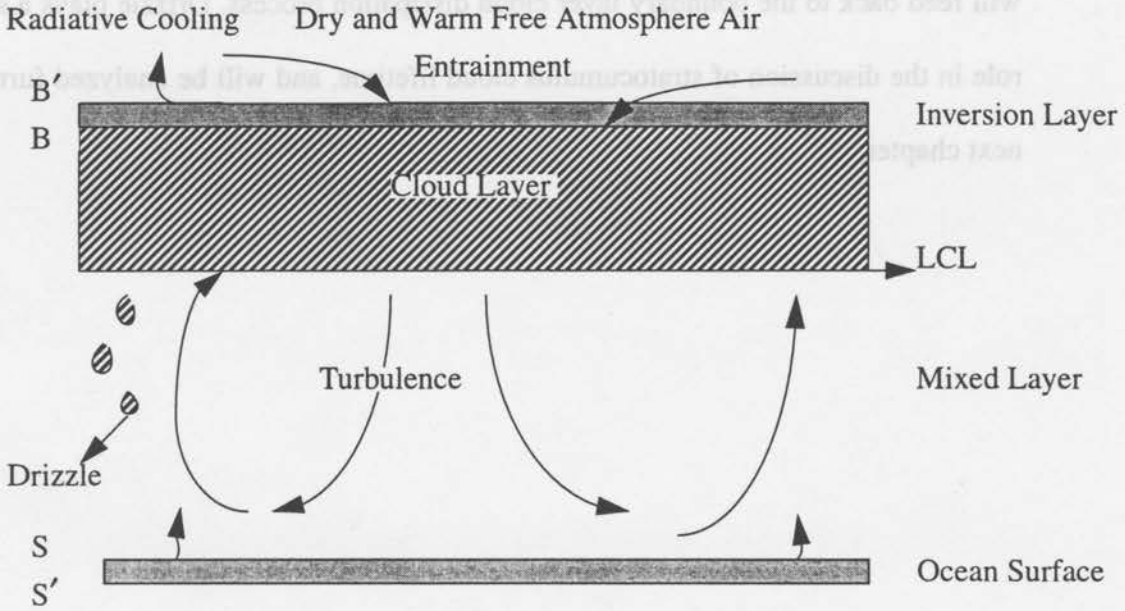

Fig. 3.1. A Schematic Diagram of a Stratocumulus Cloud Capped MBL.

The ocean is assumed to be horizontally homogeneous except for possible sea surface temperature gradients. The boundary layer is separated into four main layers: surface layer, mixed layer (including cloud layer), inversion layer (also called entrainment layer) and free atmosphere layer (Fig. 3.1). The surface layer is the layer within tens of meters above the sea surface in which turbulence follows the surface layer similarity theory (Kolmogorov, 1941; Obukhov, 1941). The mixed layer is the main part of the boundary layer and is full of turbulent motion. The inversion layer between B and B′ is assumed to be infi-

nitely thin. Level B is within the turbulence, while B′ is above the turbulence. Air above the inversion layer is dry, warm and non-turbulent. Air within the boundary layer is normally wet, cool and turbulent. Turbulent eddies penetrate into the inversion layer and engulf the free atmosphere air into the boundary layer. Thus, a sharp discontinuity exists at the interface of the inversion layer and the free atmosphere. Fig. 3.2 shows some sounding profiles from ASTEX (Wang and Albrecht, 1994). However, because the boundary layer top is hard to locate exactly, the jump values are difficult to define.

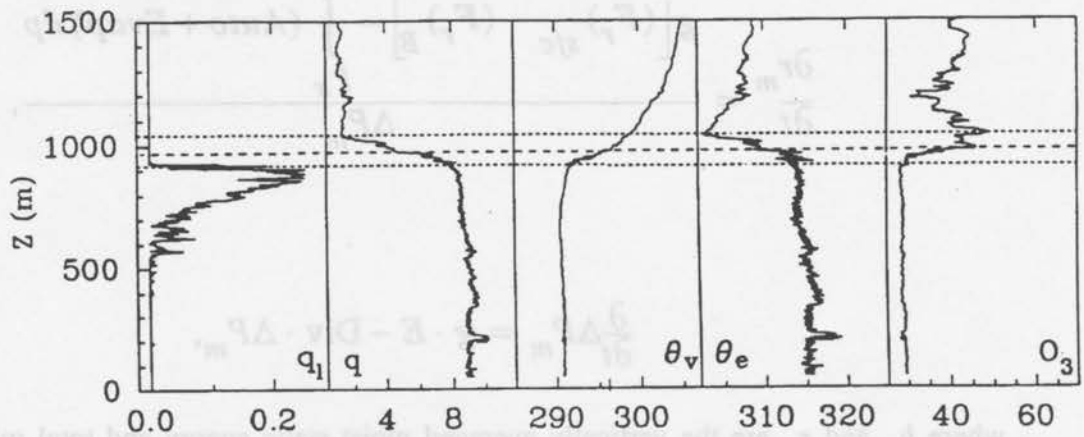

Fig. 3.2. Aircraft sounding profiles of several variables. The two horizontal short dashed lines denote the inversion layer top and base. The long dashed line denotes the level from where θ_e, q_t, and O_3 were chosen to represent the average inversion air properties (scanned from Wang and Albrecht, 1994).

It is also assumed that the stratocumulus cloud is distributed uniformly, which means there are no holes in the cloud layer and the cloud base is uniform at a single height. This height is the lifting condensation level (LCL) which is defined as the level where total water mixing ratio (r_m) equals the saturation mixing ratio (q_s). In the cloud layer, the cloud water content (q_l) equals r_m- q_s which is assumed to vary linearly with

height. This is consistent with the observation shown in panel one in Fig. 3.2.

3.2. Prognostic Equations

Based on the assumption of horizontal homogeneity, and neglecting external forcing for simplicity, integrating the conservation equations of mass, moisture and moist static energy (Appendix A) and averaging, the following equations are obtained:

$$\frac{\partial h_m}{\partial t} = \frac{g}{\Delta P_m}\left[(\boldsymbol{F_h})_{sfc} + \cancelto{0}{R_s} - (\boldsymbol{F_h})_B - \cancelto{0}{R_B}\right], \tag{3.1}$$

$$\frac{\partial r_m}{\partial t} = \frac{g\left[(\boldsymbol{F_r})_{sfc} - (\boldsymbol{F_r})_B\right] - \int_{P_B}^{Ps'} (Auto + Evap)\, dp}{\Delta P_m}, \tag{3.2}$$

$$\frac{\partial}{\partial t}\Delta P_m = \boldsymbol{g} \cdot \boldsymbol{E} - \mathrm{Div} \cdot \Delta P_m, \tag{3.3}$$

where h_m and r_m are the vertically averaged moist static energy and total mixing ratio, respectively. Note that the total mixing ratio, r_m, does not include the rainwater content q_r -- that is, $r_m = q_v + q_l$, where q_v is water vapor mixing ratio and q_l is the cloud water content. ΔP_m is the boundary layer depth. $(\boldsymbol{F_h})_{sfc}$ and $(\boldsymbol{F_r})_{sfc}$ are the moist static energy flux and moisture flux at the surface. $(\boldsymbol{F_h})_B$ and $(\boldsymbol{F_r})_B$ are the turbulent fluxes at the top (Level "B" as indicated in Fig. 3.1) of the boundary layer. In this paper, all of the vector variables are in bold.

$\boldsymbol{R_s}$ is the net surface longwave radiation flux. The radiation budget at the sea surface comes from both low cloud emission of downward longwave radiation and upward

surface emission of longwave radiation. Since the low cloud temperature is nearly the same as the sea surface temperature, it is reasonable to set R_s=0 for simplicity. R_B is the net radiation flux at the cloud top which is zero (see Fig. 2.2).

The calculation of the turbulent fluxes will be discussed in Section 3.5. *Auto* (auto-conversion) and *Evap* (evaporation) are the effects of drizzle, which will be discussed in Section 3.8. g is the acceleration of gravity. Eqn. (3.1) indicates that without the external forcing, the moist static energy budget is a balance between the surface and the top thermodynamic energy fluxes. The last integral term in eqn. (3.2) is a sink of boundary layer moisture due to precipitation. In eqn. 3.3, E represents the entrainment mass flux at the top of the boundary layer. The calculation of E is discussed in Appendix B. $Div=\nabla\bullet v$, is the large scale divergence, which is prescribed in the model. Eqn. (3.3) describes the boundary layer air mass conservation. Air entrained from above will be diverged to the sides in order to maintain a balance.

3.3. Finite Difference Scheme

A backward implicit time-differencing scheme, which is appropriate for physically damping process. A decay equation like

$$\frac{\partial q}{\partial t} = -\kappa q \ , \ \kappa>0, \tag{3.4}$$

arises in connection with many physical processes, for example, in this model, the moisture or the moist static energy budget. This is not apparent in eqns. (3.1) and (3.2). However, if the first term in both equations is expanded and rearranged, relations like those shown in eqn. (3.4) can be obtained.

The exact solution of eqn. (3.4) is:

$$q(t) = q(0)\, e^{-\kappa t}. \tag{3.5}$$

The solution indicates that q exponentially decays with time, that is, as $t \rightarrow \infty$, $q \rightarrow 0$.

Using the backward implicit scheme, eqn. (3.4) may be written in finite-difference form as:

$$\frac{q^{n+1} - q^n}{\Delta t} = -\kappa q^{n+1}, \tag{3.6}$$

where the superscript represents the time level. Superscript n represents the present time level while superscript $n+1$ represents the next time level. Δt indicates the time step. Rearranging eqn. (3.6), one obtains:

$$q^{n+1} = \frac{q^n}{1 + \Delta t \kappa}. \tag{3.7}$$

Therefore, $q^{n+1} < q^n$. This scheme is unconditionally stable.

Now, eqns. (3.1)-(3.3) in finite difference form are:

$$\frac{(h_m)^{n+1} - (h_m)^n}{\Delta t} = \frac{g}{\Delta P_m} \left((\boldsymbol{F_h})_{sfc} \right)^{n+1} + \frac{g}{\Delta P_m} \left(\boldsymbol{E}^n \left(h_{top} - (h_m)^{n+1} \right) - \Delta \boldsymbol{R} \right) \tag{3.8}$$

$$\frac{(r_m)^{n+1} - (r_m)^n}{\Delta t} = \frac{g}{\Delta P_m}\left((F_r)_{sfc}\right)^{n+1}$$

$$+\left(gE^n(h_{top} - (h_m)^{n+1}) - \left(\int_{P_B}^{P_S} (Auto + Accre + Evap)\, dp\right)^n\right)/\Delta P_m, \tag{3.9}$$

and

$$\frac{(\Delta P_m)^{n+1} - (\Delta P_m)^n}{\Delta t} = g \cdot E^n - \mathrm{Div} \cdot (\Delta P_m)^{n+1} \quad . \tag{3.10}$$

The terms without superscripts are not direct functions of the dependent variables. Hence, they are constants at a given time level n. The entrainment rate, E, are calculated at the present time level, n. $(F_h)_{sfc}$ and $(F_r)_{sfc}$ are the surface moist static energy flux and surface moisture flux, defined in the following section.

3.4. Turbulence Fluxes

3.4.1 Surface Fluxes

The surface layer is the lowest tens of meters of the boundary layer. In the surface layer, shear-driven turbulence usually is dominant. However, in a calm wind case such as in a noontime desert in a hot summer, solar radiation is very strong. There is no shear and the buoyancy-driven turbulence is dominant in the surface layer. Up into the mixed layer, the mean wind is nearly uniform with height, i.e., the mean wind shear is weak. Instead, buoyancy driven convection drives the turbulence.

The effective length scale in the surface layer is the Monin-Obukhov length scale.

The surface shear-driven turbulence is not sufficient to maintain the 500 --1000 meter thick mixed layer. This discussion is consistent with the analysis in Chapter 2, which indicates that the mixed layer turbulence is driven by radiative cooling from cloud top and causes the free-atmosphere air to be entrained into the mixed layer.

The ocean surface is the major source of moisture and sensible heat for the upper air. In this model, the surface fluxes are calculated using the bulk aerodynamic formula, which are:

$$(F_r)_{sfc} = \rho_{air}(\overline{r'w'}) = \rho_{air} C_T V (r_{sfc} - r_m), \tag{3.11}$$

$$(F_h)_{sfc} = \rho_{air}(\overline{h'w'}) = \rho_{air} C_T V (h_{sfc} - h_m), \tag{3.12}$$

where $(F_r)_{sfc}$ and $(F_h)_{sfc}$ are the surface moisture flux and surface moist static energy flux, r_{sfc} is the saturation mixing ratio at the surface air temperature and pressure. h_{sfc} is the surface moist static energy. Here it is assumed that the air just above the sea surface is saturated. V is the surface mean wind speed. C_T is the bulk aerodynamic coefficient, which is used in the same way as Bretherton et al (Garratt 1977):

$$C_T = (0.75 + 0.067|V|) \times 10^{-3} - 0.2 \times 10^{-3}, \tag{3.13}$$

where V is the lowest-leg mean wind speed. The last term on the RHS of eqn. 3.13 is a correction constant for aircraft measurement not being at 10 m. This bulk transfer law fails in calm wind conditions.

3.4.2 Turbulent Fluxes at the Cloud Top

Fluxes across the boundary layer top behave similar to those from the surface. The

only difference is that the surface is a real physical boundary, with no air mass transfer through the ocean surface, while air from above the boundary layer top can be engulfed into the boundary layer. Therefore, it is easy to relate the turbulent fluxes to the entrainment mechanism at the cloud top.

Appendix B shows that fluxes at the cloud top, which can be derived from Leibniz's theorem, are:

$$(F_r)_B = -E\Delta r = -E\,(r_{B'} - r_m), \tag{3.14}$$

$$(F_h)_B = -E\Delta h + \Delta R = -E\,(h_{B'} - h_m) + \Delta R, \tag{3.15}$$

where $r_{B'}$ and $h_{B'}$ are the free atmosphere total mixing ratio and moist static energy just above the cloud top, and ΔR is the radiation flux jump at the interface.

3.4.3 Turbulent Flux Profiles

From the Reynolds averaged equation of moist static energy, we have:

$$\frac{\partial h}{\partial t} = -\nabla\bullet(hv) - \frac{\partial}{\partial p}\omega h + g\frac{\partial}{\partial p}((F_h + R)), \tag{3.16}$$

where $\nabla\bullet$ refers to the horizontal divergence. ω is the large scale vertical velocity, and R is the net radiation flux. Reorganizing the equation above with the Boussinesq approximation of mass continuity,

$$\nabla\bullet v + \frac{\partial \omega}{\partial p} = 0, \tag{3.17}$$

and also assuming horizontal homogeneity, $\nabla h = 0$, and a well-mixed layer, $\frac{\partial h}{\partial p} = 0$, one obtains

$$\frac{\partial h}{\partial t} = g\frac{\partial}{\partial p}(\boldsymbol{F_h} + \boldsymbol{R}) \ . \tag{3.18}$$

Taking the derivative of (3.15) with respect to pressure, we may got

$$\frac{\partial}{\partial p}(\frac{\partial h}{\partial t}) \ = \frac{\partial}{\partial t}(\frac{\partial h}{\partial p}) \ = 0 = g\frac{\partial^2}{\partial p^2}(\boldsymbol{F_h} + \boldsymbol{R}), \tag{3.19}$$

which means:

$$\frac{\partial}{\partial p}(\boldsymbol{F_h} + \boldsymbol{R}) \ = \text{constant}. \tag{3.20}$$

Following a similar procedure, one obtain:

$$\frac{\partial \boldsymbol{F_r}}{\partial p} \ = \text{constant}. \tag{3.21}$$

eqn. (3.20) and (3.21) indicate that $\boldsymbol{F_h}$+$\boldsymbol{R}$ and $\boldsymbol{F_r}$ are independent with height. Following the discussion of Chapter 2, $\boldsymbol{R}$=*0* is assumed at any level below the cloud top. Therefore, from (3.20) and (3.21), $\boldsymbol{F_h}$ and $\boldsymbol{F_r}$ may be computed at any height:

$$\boldsymbol{F_h}(p) \ = \ (\boldsymbol{F_h})_s\left(\frac{p - p_B}{\Delta P_m}\right) + (\boldsymbol{F_h})_B\left(\frac{p_s - p}{\Delta P_m}\right), \tag{3.22}$$

and

$$\boldsymbol{F_r}(p) \ = \ (\boldsymbol{F_r})_s\left(\frac{p - p_B}{\Delta P_m}\right) + (\boldsymbol{F_r})_B\left(\frac{p_s - p}{\Delta P_m}\right). \tag{3.23}$$

3.5. Turbulence Kinetic Energy Budget

3.5.1 Conservation Equations for the Turbulence Kinetic Energy (TKE)

The mean turbulence kinetic energy (TKE) is defined as:

$\bar{e} = \frac{1}{2} \times (\overline{u'^2} + \overline{v'^2} + \overline{w'^2})$, with dimensions of velocity squared. The TKE budget equation can be derived under the horizontal homogeneity assumption (Stull, 1988):

$$\frac{\partial \bar{e}}{\partial t} + \bar{w}\frac{\partial \bar{e}}{\partial z} = \frac{g}{\theta_v}\overline{(w'\theta'_v)} - \overline{u'w'}\frac{\partial \bar{u}}{\partial z} - \frac{\partial}{\partial z}\overline{(w'\bar{e})} - \frac{1}{\rho}\frac{\partial}{\partial z}\overline{(w'p')} - \varepsilon. \quad (3.24)$$

(1) (2) (3) (4) (5) (6) (7)

Term (1) Local tendency of TKE
Term (2) Vertical advection of TKE
Term (3) Buoyancy production
Term (4) Shear production
Term (5) Turbulent transport of TKE
Term (6) Pressure perturbation by gravity waves
Term (7) TKE dissipation

Vertically integrating (3.24) and using Leibniz's rule, One obtains (Randall. et.al., 1992):

$$\frac{\partial e_m}{\partial t} = \frac{g}{\Delta P_m}(S + B - Ee_m - D), \quad (3.25)$$

where e_m is the vertically integrated mean TKE. D is the dissipation rate of turbulence kinetic energy, which is assumed to satisfy:

$$D = \rho\left(\frac{e_m}{a_1}\right)^{\frac{3}{2}}. \quad (3.26)$$

This is based on Deardorff's (1974) LES results, which suggested a_1=*0.163*.

B represents the buoyancy production rate, which is

$$B = \kappa \int_{p_{B'}}^{p_{s'}} \frac{F_{sv}}{p} dp, \quad (3.27)$$

where κ is Poisson's constant, equal to 0.286

When an air parcel is warmer than the ambient air, it will be positively buoyant and accelerate upward. Similarly, if an air parcel is colder than the ambient air, it will be negatively buoyant and accelerate downward. In these two cases, mean potential energy is converted to TKE. On the other hand, if an air parcel is warmer (colder) than the ambient air, if the initial velocity anomaly is downward (upward), the air parcel will be decelerated. TKE is converted to mean potential energy (Randall, 1984a). Each parcel is considered as either producing TKE or consuming TKE (Stage and Businger, 1981). Therefore, the buoyancy production rate is obtained by the summation over all the parcel contributions within the boundary layer.

Once the vertical profile of buoyancy flux, $\mathbf{F_{sv}}$, is known, the integration of (3.24) can be solved. The buoyancy flux is related to the turbulent moist static energy and moisture flux and can be computed from (Schubert, 1976; Randall, 1980a):

$$F_{Sv} = F_h - (1 - \delta\varepsilon) LF_r, \qquad \text{for clear air} \qquad (3.28)$$

$$F_{Sv} = \beta F_h - \varepsilon LF_r, \qquad \text{for cloudy air} \qquad (3.29)$$

where

$$\varepsilon = \frac{C_p T}{L}, \delta = 0.608, \beta = \frac{[1 + (1 + \delta)\gamma\varepsilon]}{(1 + \gamma)}, \gamma = \frac{L}{C_p}\left(\frac{\partial}{\partial T} q^*\right)_p, \qquad (3.30)$$

C_p is heat capacity, L is the water vapor latent heat constant, T is the temperature at any level p, and q^* is the saturation mixing ratio.

S represents the shear production rate:

$$S = \int_{p_{B'}}^{p_{S'}} \vec{F}_{\vec{v}} \bullet \frac{\partial \vec{V}}{\partial p} dp, \tag{3.31}$$

where $\vec{F}_{\vec{v}}$ is the horizontal momentum flux in vector form. $\vec{V}$ is the horizontal velocity. The shear production rate represents the process of the conversion of mean kinetic energy to TKE. Shear is weak in the unstable PBL, but is dominant in the stably stratified PBL. Shear production can be divided into three parts: shear production in the surface layer, shear production inside the boundary layer, and shear production in the entrainment layer. In the mixed-layer model, the wind is constant inside the boundary layer, so there is no shear contribution from the mixed-layer. The contributions come from the surface layer and the entrainment layer only. Therefore, eqn. (3.31) can be rewritten:

$$S = \int_{p_s}^{p_{s'}} \vec{F}_{\vec{v}} \bullet \frac{\partial \vec{V}}{\partial p} dp + \int_{p_{B'}}^{p_B} \vec{F}_{\vec{v}} \bullet \frac{\partial \vec{V}}{\partial p} dp = \left| (\boldsymbol{F}_v)_s \right| |\boldsymbol{V}_m| + \frac{1}{2} \boldsymbol{E} |\Delta \overline{\boldsymbol{V}}|^2, \tag{3.32}$$

where the first term is the surface layer contribution, assuming that the surface momentum fluxes are parallel to the surface mean wind, and the second term is the entrainment layer contribution. ΔV is the wind velocity jump at the top of the MBL. The factor of *1/2* comes from the averaging of the momentum flux within the entrainment layer.

3.5.2 Solution of the TKE Equation

Eqn. (3.25) in finite difference form is:

$$e_m^{n+1} - e_m^n = \frac{g \Delta t}{\Delta P_m} \left(\boldsymbol{S} + \boldsymbol{B} - \boldsymbol{E}^n e_m^{n+1} - \rho \left(\frac{e_m^{n+1}}{a_1} \right)^{\frac{3}{2}} \right), \tag{3.33}$$

where the superscript represents the time level. Also, note here that the entrainment rate use forward scheme for simplicity. Letting $x = (e_m^{n+1})^{\frac{1}{2}}$, and rearranging eqn. (3.33), one obtains:

$$x^3 + a_2 x^2 + a_1 x + a_0 = 0 \quad , \tag{3.34}$$

where a_2, a_1 and a_0 are constant coefficients that can be calculated. This cubic equation can be solved, choosing the root which is always real, to obtain the solution for e_m^{n+1}.

3.6. Entrainment Parameterization

As discussed in Appendix B, the entrainment mass flux can be expressed as:

$$E = \rho \left(\frac{\partial z_B}{\partial t} + \bar{v}_B \nabla z_B - \bar{w}_B \right) . \tag{3.35}$$

A parameterization of the entrainment rate is needed to close the mixed layer problem.

The most popular method used is the flux-ratio method (Ball, 1960). For the free convection case, the buoyancy fluxes at the top of the mixed layer and at the surface are related by:

$$-(\overline{w'\theta'_v})_B = A \cdot (\overline{w'\theta'_v})_S , \tag{3.36}$$

where A is normally set to 0.2, which is a good approximation for free convection in the clear sky case (Stull, 1976a). Thus, the entrainment rate can be expressed as:

$$E = \frac{0.2\,(\overline{w'\theta'_v})_S}{\Delta\theta_v} . \tag{3.37}$$

Eqn. (3.37) does not fit properly for the cloudy case in which the "0.2" relation

does not hold. However, it is very natural to relate the entrainment process to the mixed layer turbulence directly. When the turbulence is strong, more eddies will penetrate at the interface and more air will be entrained, and vice versa. This is the idea that suggests the turbulence kinetic energy be connected in some way to the entrainment rate.

Deardorff(1980) gives an entrainment velocity (not mass flux) formula:

$$\frac{w_e}{w^*} = R_i^{*-1}, \tag{3.38}$$

where $R_i^* = \frac{g}{\Theta_0}\frac{z_i \Delta\Theta}{w^{*2}}$ is called the buoyancy Richardson number. w^* is Deardorff's mixed layer vertical velocity scale: $w^* = (\frac{g}{T_0}\overline{w\theta_0} z_i)^{\frac{1}{3}}$.

The relation above is derived for the clear sky situation. Starting from eqn. (3.38), the entrainment rate is rewritten as a function of the TKE, e_m, as follows (Krasner, 1993):

$$E = \rho w_e = \rho \sqrt{e_m} \frac{b_1}{(1 + b_2 R_i)}, \tag{3.39}$$

where $R_i = \frac{g}{\bar{\theta}_v}\frac{\Delta\overline{\theta}_v z_i}{e_m}$ is the relevant Richardson number and noticing the difference between eqns. (3.38) and (3.39), $w^* \sim \sqrt{e_m}$, $w^{*2} \sim e_m$. From eqn. (3.39), if $e_m=0$, $E=0$. That is, if there is no turbulence, there will be no entrainment. Also, notice that here the entrainment rate is always positive. Actually, entrainment can be negative, which means air is detrained from the boundary layer.That might happen when the boundary layer grow rapidly. In that case, the formula will be different (Krasner, 1993). In this model, we assume that entrainment rate are always positive. Thus, air in the free atmosphere can be entrained into the boundary layer and air inside of the boundary layer can not be detrained.

3.7. Drizzle Parameterization

Drizzle formation is a cloud microphysical process starting from the growth of cloud condensation nuclei (CCN). Under supersaturated conditions, CCN activated and grow to small cloud droplets by condensation. Small cloud droplets further collect cloud liquid water and grow to become large droplets. When the droplets are large enough, they rain out.

For typical marine stratiform clouds, the supersaturation might be more than 0.1%, which means generally that particles with diameters larger than about 0.1 μm can be activated into cloud droplets (Baker and Charlson, 1990). Since a parameterization of drizzle is the main goal, the details of CCN-to-cloud droplet growth process are neglected here. In this model, however, supersaturations are not computed. Instead, it is assumed that all of the CCN in the cloud layer are activated. Thus, in that layer, the cloud droplet number concentration equals the CCN number concentration.

In order to study the relationship among CCN, cloud droplets and drizzle production, the cloud droplet number concentration is assumed to follow a modified gamma distribution:

$$n(D) = \frac{dN}{dD} = N_0 D^{\mu} exp(-\lambda D), \tag{3.40}$$

as plotted in Fig. 3.3. N_0 is proportional to the total number concentration, $[N_{CCN}]$; μ is the shape parameter, which defines the spectrum width and spectrum height of the distribution function; λ is the slope parameter, such that λ^{-1} represents the characteristic diameter. It is assumed that the cloud droplet distribution does not change with height so that

the shape parameter μ is fixed. Large value of μ corresponds to a narrow spectrum, while a small value of μ represents a broad spectrum. For $\mu = 0$, the distribution function becomes the Marshall-Parmer exponential distribution, $n(D) = N_0 exp(-\lambda D)$. According to observational studies by Levin (1958) and Clark (1974), the shape parameter μ for cloud droplets is in the range between 5 to 9. Thus, μ equal to 6 is chosen for this study.

If the total cloud droplet concentration, $N_{cld}=N_{CCN}$, and the total liquid water mixing ratio, q_l, are known, then N_0 and λ may be obtained by solving

$$N_{CCN} = \int_0^\infty n(D)\, dD = \int_0^\infty N_0 D^\mu e^{-\lambda D} dD = \frac{N_0}{\lambda^{\mu+1}} \Gamma(\mu+1), \quad (3.41)$$

and

$$q_l = \int_0^\infty n(D) \frac{\pi}{6} D^3 \frac{\rho_{water}}{\rho_{air}} dD = \frac{\pi}{6} \frac{\rho_{water}}{\rho_{air}} \frac{N_0}{\lambda^{\mu+4}} \Gamma(\mu+4), \quad (3.42)$$

where $\Gamma()$ refers to the gamma function. Since N_{CCN} and q_l are two time-dependent variables, different values of N_0 and λ may be obtained for different N_{CCN} and q_l at each time step:

$$\lambda = \left(\frac{\pi}{6} \frac{\rho_{water}}{\rho_{air}} \frac{\Gamma(\mu+4)}{\Gamma(\mu+1)} \frac{N_{CCN}}{q_l} \right)^{\frac{1}{3}}, N_0 = \frac{N_{CCN} \lambda^{\mu+1}}{\Gamma(\mu+1))}. \quad (3.43)$$

Thus, strictly speaking, the number distribution function *n(D)* should be written as $n(N_{CCN}, q_l, D)$.

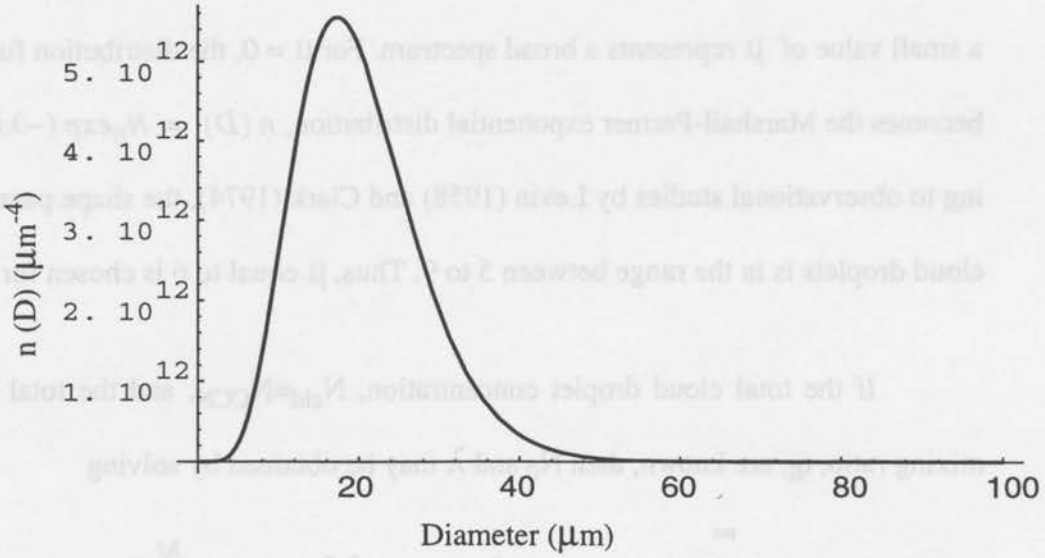

Fig. 3.3. A gamma number distribution of cloud droplets with the shape parameter, μ=6 for q_l = *0.5* g kg^{-1} and [N_{CCN}] = 100 cm^{-3}.

Drizzle physics, ignoring the condensational growth process, include three key processes: autoconversion, accretion and evaporation. One of the model assumptions is that no supersaturated water vapor exists inside the cloud. In other words, it is assumed that when the water vapor concentration reaches saturation, any excess converted to cloud liquid water immediately. Thus, condensation is not explicitly treated in this model. Autoconversion is the process through which small cloud droplets collide with each other and coalesce into bigger droplets. Further, bigger droplets collect the ambient cloud droplets and grow to rain drops. This is the accretion process. After falling out of the cloud layer, the raindrops begin to evaporate because the below-cloud ambient air is unsaturated. That is the evaporation process.

Autoconversion is the crucial starting point for drizzle production. However, the understanding of this process is still poor. Kessler (1969) first gave a parameterization

sion threshold. In Baker's model, the critical radius was interpreted as the mean size of the cloud droplet number distribution instead of the threshold for significant coalescence to occur. When the mass mean cloud droplets radius is greater than 10 μm, the autoconversion process begins. Otherwise, it is shut off. Baker's method is an improvement on Chen and Cotton's because the CCN number concentration does not need to be fixed. A relation between the critical radius, r_{cr} and the CCN number concentration has been developed.

Gerber (in press) assumed that the heavy drizzle observed in ASTEX stratocumulus clouds was due to a relatively large number of cloud droplets which have grown past the coalescence radius threshold by condensation.

A method for determining the autoconversion rate which is a mixture of the above ideas is proposed here. The critical threshold for liquid water content, q_{cr}, should be a function of the cloud droplet number concentration ($[N_{CCN}]$). This relation can be obtained by assuming that the drizzle process is switched on if the number concentration of the large droplets is a relatively large fraction of the total cloud droplet number concentration, $[N_{CCN}]$.

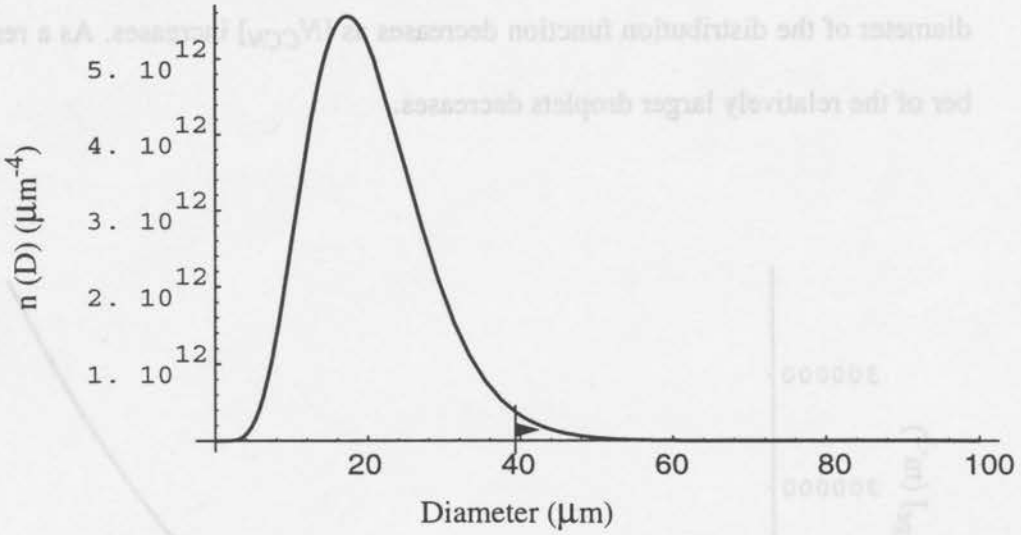

Fig. 3.4. A Gamma number distribution with shape parameter, μ=6. The vertical bar indicates the critical diameter, D_{cr} = *38* μ*m*. The arrow denotes the direction of integration.

The definition of α is

$$\alpha = \frac{\left[N_{large}\left(N_{CCN}, q_l\right)\right]}{\left[N_{CCN}\right]}, \tag{3.46}$$

where $[N_{large}(N_{CCN}, q_l)]$ is the number concentration of droplets with diameters larger than the critical value, D_{cr} (Fig. 3.4). When α is greater than a critical value, α_{cr}, which will be defined later, the autoconversion process will start. Otherwise, it will be shut off.

Fig. 3.5 indicates that at a fixed $[N_{CCN}]$, while increasing liquid water content, N_{large} increases monotonically, because the mean diameter of the distribution shifts towards the larger droplet size. However, for increasing $[N_{CCN}]$ and fixed liquid water content, when the total cloud droplet number concentration is low, the distribution is shifted toward larger drops and the number concentration of droplets with diameters larger than D_{cr} increases as the total number concentration increases. When $[N_{CCN}]$ is

high, the liquid water content is not sufficient to allow many large drops, and the mean diameter of the distribution function decreases as $[N_{CCN}]$ increases. As a result, the number of the relatively larger droplets decreases.

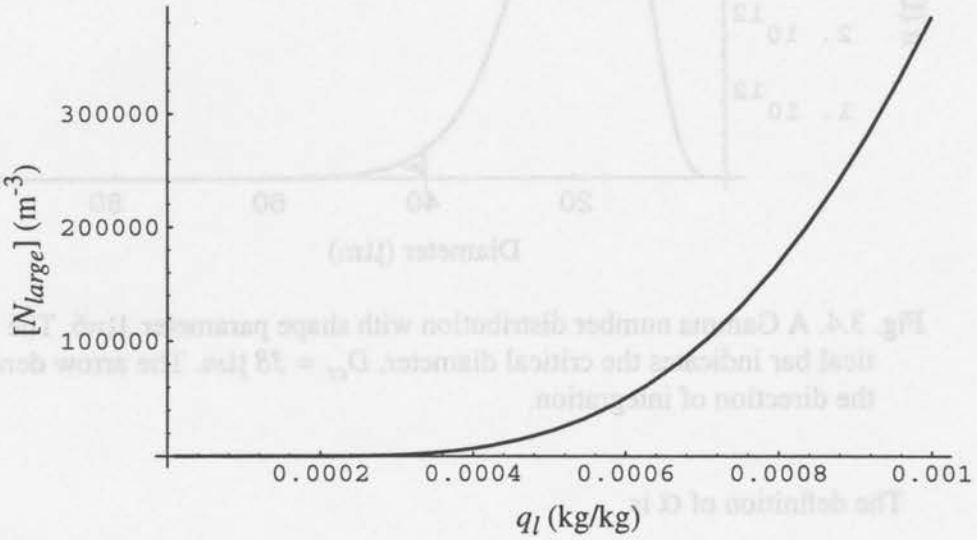

Fig. 3.5. $[N_{large}]$ is as a function of cloud liquid water at a fixed $[N_{CCN}]$, $[N_{CCN}]$= 100 cm^{-3}; 0.01 g kg^{-1} < q_l < 10 g kg^{-1}; and D_{cr} =38 μm.

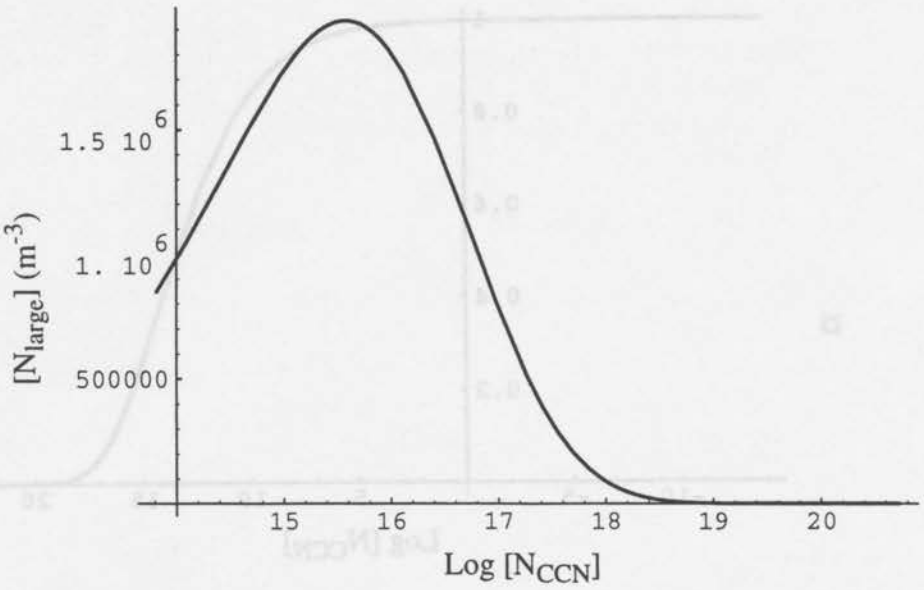

Fig. 3.6. $[N_{large}]$ versus $[N_{CCN}]$ at a given q_l, q_l=0.5 g kg^{-1}. 10^{-12} cm^{-3} < $[N_{CCN}] < 10^4$ cm^{-3} and the critical diameter, D_{cr} = 38μm.

Based on the proceeding analysis, for a fixed the coalescence threshold diameter, α is a function of q_l and $[N_{CCN}]$ [see eqn. (3.46)]. For a given q_l, when the CCN number concentration is very low, α goes to 100%, indicating that all of the CCN are large droplets. On the other hand, when too many CCN exist, α goes to zero for the available liquid water is distributed over many small drops (Fig. 3.7).

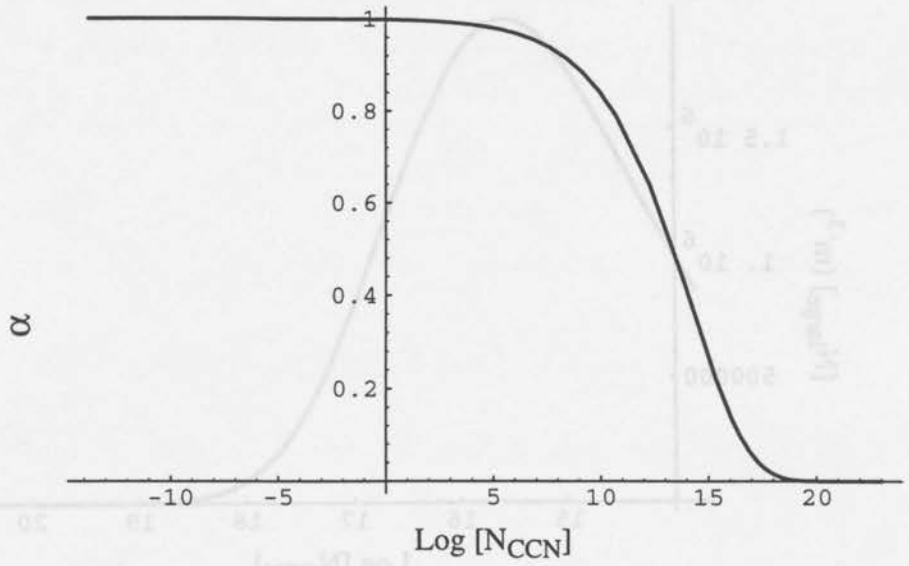

Fig. 3.7. Ratio of $[N_{large}]$ to the total cloud droplet number concentration plotted as a function of $[N_{CCN}]$, for fixing $q_l = 0.5$ g kg^{-1}, in the range 1 cm^{-3}< $[N_{CCN}]$ < 1000 cm^{-3}.

$N_{large}\,(N_{CCN}, q_l)$ can be written as:

$$N_{large}\,(N_{CCN}, q_l) = \int_{D_{cr}}^{\infty} n\,(N_{CCN}, q_l, D)\,dD = N_{CCN} - \int_{0}^{D_{cr}} n\,(N_{CCN}, q_l, D)\,dD. \quad (3.47)$$

Then, eqn.(3.46) may be rewritten as:

$$\alpha = 1 - \frac{\int_{0}^{D_{cr}} n\,(N_{CCN}, q_l, D)\,dD}{N_{CCN}} = 1 - \int_{0}^{D_{cr}} \frac{\lambda^7}{\Gamma(7)} D^6 e^{-\lambda D} dD \quad . \quad (3.48)$$

A critical value of α_{cr}=0.01 is assumed in this model. If $\alpha > \alpha_{cr}$, which means that more than 1% of the total cloud droplet number concentration falls in the significant coalescence range, then autoconversion starts. Otherwise, no rain is produced. Thus, a relation between $[N_{CCN}]$ and q_{cr} is obtained:

$$\alpha_{cr} = 1 - \frac{\int_0^{D_{cr}} n(N_{CCN}, q_{cr}, D)\, dD}{N_{CCN}} = 1 - \int_0^{D_{cr}} \frac{\lambda_{cr}^7}{\Gamma(7)} D^6 e^{-\lambda_{cr} D} dD \quad , (3.49)$$

where

$$\lambda = \left(\frac{\pi}{6} \frac{\rho_{water}}{\rho_{air}} \frac{\Gamma(11)}{\Gamma(7)} \frac{N_{CCN}}{q_{cr}} \right)^{\frac{1}{3}},$$

and q_{cr} represents the minimum cloud water content at a given cloud droplets number concentration [N_{CCN}] to allow 1% (which is α_{cr}) of the total cloud droplets to fall into the coalescence region. When $q_l > q_{cr}$, $\alpha_l > \alpha_{cr}$. The autoconversion begins. Otherwise, autocoversion shuts off.

Notice that in eqn.(3.43), λ is only a function of $\left(\frac{N_{CCN}}{q_l}\right)$. Solving eqn. (3.49) is identical to finding a value of $\left(\frac{N_{CCN}}{q_l}\right)$ that can make the RHS of eqn. (3.48) equal to α_{cr}. A plot of α versus $\left(\frac{N_{CCN}}{q_{cr}}\right)$ from eqn. (3.48) is shown in Fig. 3.8, and indicates that there is only one real root to satisfy eqn. (3.49), or in other words, to satisfy $\alpha = \alpha_{cr}$ for $\left(\frac{N_{CCN}}{q_{cr}}\right)$ in the range from 0 to 10^{12}. The order of magnitude of N_{CCN} is about $10^7 \sim 10^8$ m^{-3} and q_l is around 10^{-4} kg kg^{-1}. Therefore, reasonable values of $\left(\frac{N_{CCN}}{q_{cr}}\right)$ are around $10^{10} \sim 10^{12}$ kg kg^{-1} m^{-3}.

For the case of D_{cr}=38 μm and α_{cr}=0.01, according to Fig. 3.8,

$$\frac{N_{CCN}}{q_{cr}} \cong 2.61 \times 10^{11} \text{ kg kg}^{-1} \text{ m}^{-3}, \quad (3.50)$$

while for the case of D_{cr}=20 μm and α_{cr}=0.01,

$$\frac{N_{CCN}}{q_{cr}} \equiv 1.73 \times 10^{12} \text{ kg kg}^{-1} \text{ m}^{-3}. \tag{3.51}$$

The CCN number concentration has a linear relation with the critical cloud water content for $\left(\frac{N_{CCN}}{q_{cr}}\right)$ within the practical range. The dramatic difference between the two lines in Fig. 3.8 showed the model's sensitivity to the choice of D_{cr}. This occurs since, for all of the other variables fixed, $[N_{large}]$ is larger for a wider integrating range (D_{cr}=20 μm) while it is smaller for a narrower integrating range (D_{cr}=38 μm). In order to obtain the same α_{cr}, the real root of eqn. (3.48) has to shift to a larger value.

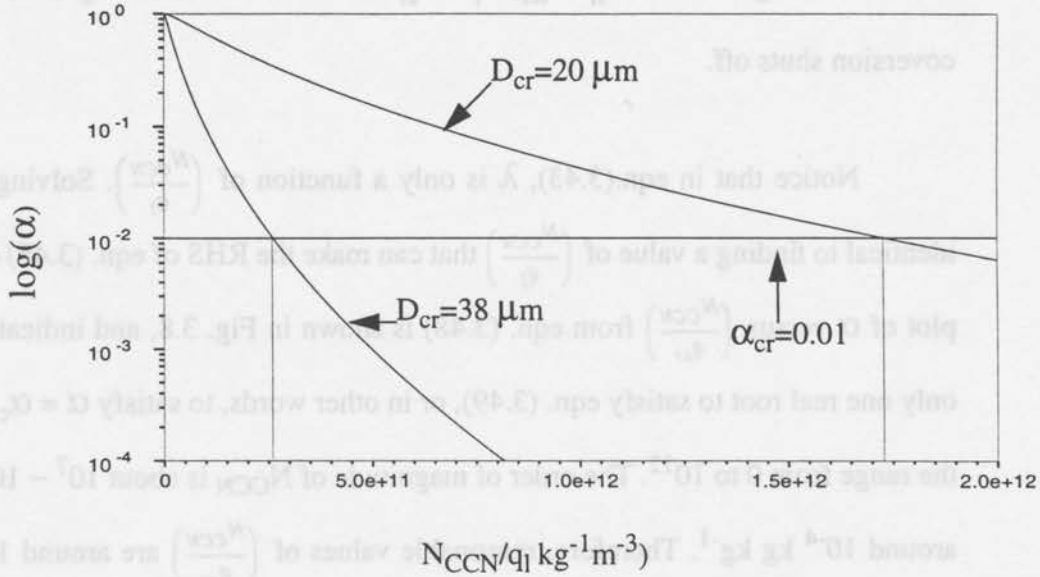

Fig. 3.8. The ratio of $[N_{large}]$ to $[N_{CCN}]$ versus $\left(\frac{N_{CCN}}{q_l}\right)$. Dashed line is using a coalescence diameter threshold of 38 μm. Dotted line is with D_{cr}=20 μm. Solid line denote the critical ratio of α for autoconversion process.

Fig. 3.9 shows the α-$\left(\frac{N_{CCN}}{q_l}\right)$ relation for different shape parameters, μ. There are no dramatic changes in the α-$\left(\frac{N_{CCN}}{q_l}\right)$ relation as μ varies. In Fig. 3.10, it is shown that although the cloud droplet size spectrum varies with the shape parameter, the number concentration for the larger cloud droplets, which is represented by the integration in diameter

space through the tail part of each distribution functions (shown by the arrow), does not vary dramatically.

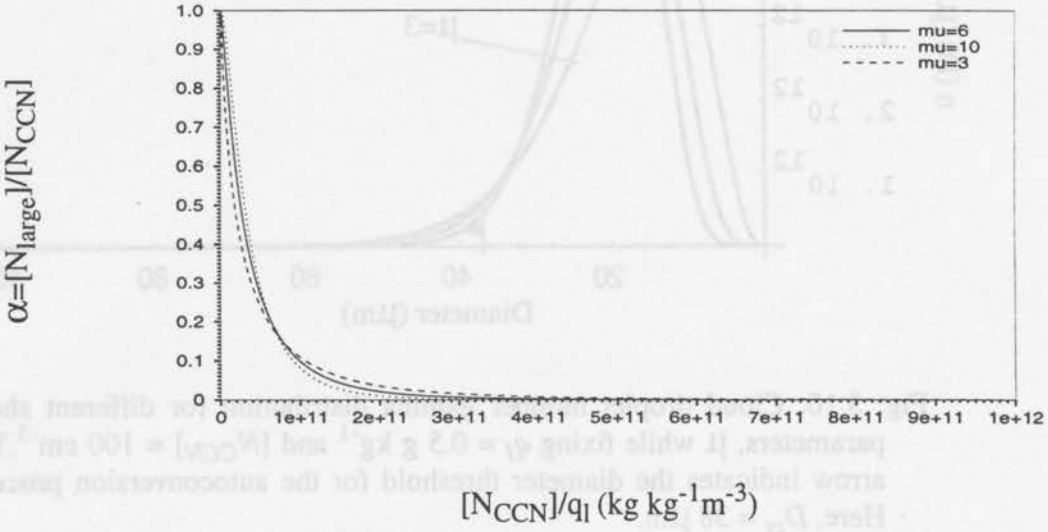

Fig. 3.9. α versus $\left(\frac{N_{CCN}}{q_l}\right)$ for different cases of cloud droplet number concentration.

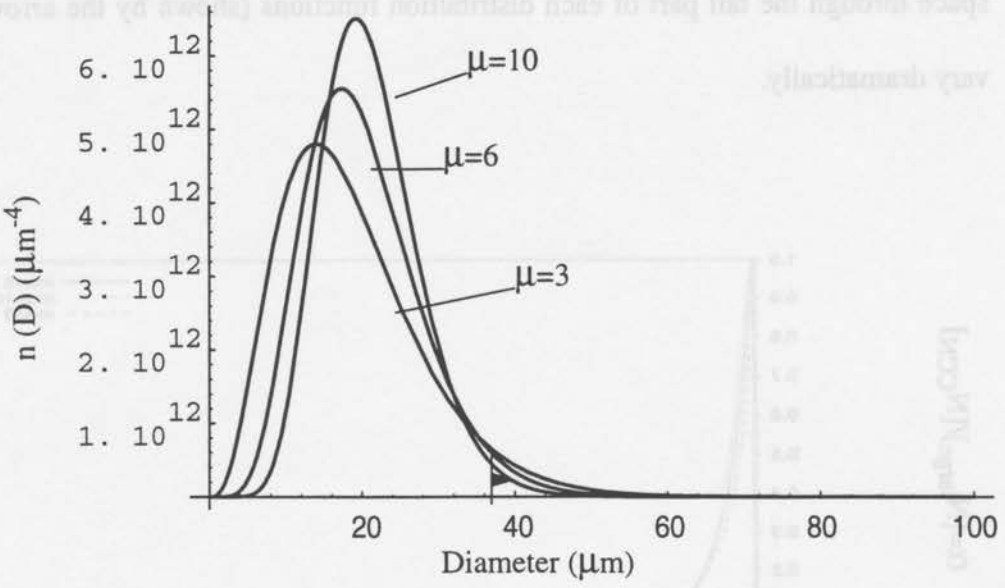

Fig. 3.10. Cloud droplet number gamma distribution for different shape parameters, μ while fixing q_l = 0.5 g kg^{-1} and [N_{CCN}] = 100 cm^{-3}.The arrow indicates the diameter threshold for the autoconversion process, Here, D_{cr} = 38 μm.

Thus, the autoconversion rate can be computed by eqn. 3.43:

$$Auto = D\,(q_l - q_{cr}),\ q_{cr} = aN_{CCN}, \tag{3.52}$$

where a=3.83 × 10^{-12} kg kg^{-1}m^3 for Gerber's case (D_{cr} = 38 μm) or a=5.78 × 10^{-13} kg kg^{-1}m^3 for Chen and Cotton's case (D_{cr} = 20 μm). As CCN number concentration decreases, the critical cloud water mixing ratio decreases. Therefore, the autoconversion rate increases since the cloud droplet radius becomes larger and more cloud droplets fall into the coalescence range.

Notice that the slope, a of the linear relation between q_{cr} and N_{CCN}, depends on the choice of the critical value of α (Fig. 8). With a smaller α_{cr}, a larger a will be obtained, and vice versa. Through the remainder of this thesis, the choice of α_{cr}will be

fixed at 0.01, thus, a=3.83e-12 kg kg^{-1}m^3.

The accretion process in the model is parameterized following Wang and Wang (1994), which is originally from Redelsperger and Sommeria (1986), based on their sub-grid turbulence parameterization in their three dimensional large eddy simulation:

$$Accre = B\, q_l\, q_r \qquad (3.53)$$

where

$$B = 1.485\left(\frac{q_r}{N_0}\right)^{-(\frac{1}{20})} \rho^{0.95} \quad , \qquad (3.54)$$

and ρ is the air density, which is assumed constant in the present model. N_0 is the intercept parameter, which can be calculated from $N_0 = N_r/R_m$, where $N_r = 2020$ m^{-3} is the raindrop number concentration. The rain-droplet number concentration is based on the Marshall-Palmer-type distribution (Tripoli and Cotton, 1980):

$$\phi(R) = N_0 exp(-\frac{R}{R_m}) = \frac{N_r}{R_m} exp(-\frac{R}{R_m}) \quad , \qquad (3.55)$$

where R_m is a characteristic drizzle droplet radius. R_m is given by Chen and Cotton (1987) as:

$$R_m = \left(\frac{q_r}{8\times 10^3 \pi N_r}\right)^{(\frac{1}{3})} . \qquad (3.56)$$

Below cloud, the evaporation process assumed here is similar to Redelsperger and Sommeria (1986) as well, that is:

$$Evap = -\, C\,(q_s - q_r)\, q_r \qquad (3.57)$$

where q_s is the saturation mixing ratio. The time scale of evaporation process is approximately several seconds, as recommended by Redelsperger and Sommeria (1986). In this model, a time scale of 2.5 seconds is assumed. Thus, the coefficient, C equals 0.4.

In this model, for simplicity, the drizzle terminal velocity, v_t, is set constant to 1 cm s^{-1}. In future work, this should be made a function of droplet size. The gravitational drizzle flux is:

$$F_d = - \rho v_t q_r \tag{3.58}$$

As a summary, a drizzle parameterization regulated by the cloud droplet number concentration is developed. The critical mass threshold of the cloud water content, q_{cr}, is linear with the cloud droplet number concentration, $[N_{CCN}]$. Results and sensitivity studies will be shown in the following two chapters.

Chapter 4

Aerosols and CCN Sources, Sinks and Transports

4.1. Previous Work on Models of Aerosols and CCN Models

Marine stratocumulus clouds are characterized by lower cloud droplet concentrations and larger droplet size compared with continental clouds. The major source of CCN in remote marine regions is believed to be dimethylsulfide (DMS), which is a metabolic by-product of marine phytoplankton. DMS fluxes enter the boundary layer from the ocean surface. The major reaction is the oxidation of DMS by hydroxyl ($OH\bullet$) radicals in the atmosphere. The major products of this reaction are methanesulfonic acid (MSA) and SO_2. SO_2 may further be oxidized to form sulfuric acid (H_2SO_4). MSA and H_2SO_4 are believed to be the major source of the mass of particulate matter which forms CCN.

Many observations show that the aerosol size distribution in the clean marine boundary layer usually has a bimodal distribution. The first mode corresponds to particles of diameter smaller than 0.12 μm, called the nucleation mode and the second mode contains particles of diameter from 0.12 to 0.6 μm which is called the accumulation mode (Quinn et al., 1993). Accumulation mode particles can grow to cloud droplets under supersaturations of a typical marine stratiform clouds case (Baker and Charlson, 1990) while the nucleation mode particles are too small to activated and grow to cloud droplets. Therefore, Pandis et al. define the accumulation mode particles as CCN particles.

Most previous modeling studies of marine aerosols have used a box-model approach, which assumes fixed temperature, pressure and relative humidity conditions. Simple chemical reactions involving sulfur species are usually assumed, which produce condensable vapors which may enter the aerosol phase. Aerosol particles form and grow by nucleation, condensation, coagulation and deposition processes. Kreidenweis and Seinfeld (1988) used a box model on the DMS-H_2O system to analyze the nucleation rate of aerosol particles by a binary nucleation theory. Pandis et al. (1994) used a box model to examine the relationship between DMS flux and CCN number concentration. The box-model approach is ideal for developing an understanding of the basic chemical and physical processes of aerosol. However, it lacks the link with the real atmosphere, where thermodynamics conditions should vary with time and space.

CCN can be activated and grow into cloud droplets for supersaturation larger than 0.1% in a typical marine stratocumulus cloud. Typical concentrations of the cloud droplet are always in the range from ten to several hundred particles per cubic centimeter in MBL. For example, results from the ASTEX (1992) study showed that the cloud droplet concentration was between 50 cm^{-3} and 150 cm^{-3} (Bretherton, 1995). These number concentrations do not vary much with season or latitude. Thus, in cloud modeling, cloud droplet concentrations have often been assumed constant. Since cloud droplets are grown from the CCN mode particles, some modelers suggest that cloud droplet number concentration be set to CCN number concentration for simplicity (Baker, 1993).

Baker and Charlson (1990) and Baker (1993) used a simple well-mixed layer model to study the aerosol-cloud interactions. They discussed the possibility of multiple

steady state CCN number concentrations in the marine boundary layer for fixed atmospheric conditions. In Baker's (1993) model, a monodisperse CCN mode was assumed. The cloud droplet number was assumed equal to the CCN number concentration. Two steady-state solutions was found to exist. One of them is [CCN]< 100 cm^{-3}, corresponding to the typical marine case. In this case, the major sink is precipitation. The other is larger than 1000 cm^{-3}, which is thought to be a continental case. It is obtained when drizzle is shut off and coagulation acts as the main sink for droplet and CCN number concentration. However, for different atmospheric conditions, steady-state [CCN] might shift.

Recent work suggests that an increase in CCN concentration may lead to a decrease in cloud droplet size if the cloud liquid water content is fixed. Higher cloud reflectivity will result, due to the increase in cloud droplet surface area. Smaller drop size may also limits drizzle formation and increase the cloud lifetime (Albrecht 1989). As an example, the phenomena of "ship tracks" observed from satellite under clear sky conditions indicate that aerosol emitted in the ship exhaust may increase the CCN concentrations, and allow a cloud line to form where ambient air is moist enough. Ackerman et al (1993), from another point of view, pointed out that if the droplet concentration is very low, the cloud may become very thin and the boundary layer turbulence which is driven by the cloud top radiative cooling will be suppressed. The cloud layer may collapse to a shallow fog layer. Thus, the variation of N_{CCN} may again affect the cloud lifetime.

4.2. Model Description of Aerosol and CCN Budget

To examine the interactions between aerosols and clouds, a simple stratocumulus cloud topped marine boundary layer model as described in the previous chapters is used to

prescribe the atmospheric thermodynamic conditions. A simple model of aerosol physics is coupled to it. Two modes of aerosol are assumed: dry particles, with a small mean diameter, correspond to nucleation mode particles in the diameter range of 0.03 μm to 0.1 μm; CCN particles correspond to larger accumulation mode particles of diameters between 0.1 μm to 0.6 μm. Aerosol concentrations respond to different thermodynamic situations, and interact with the model dynamics through the impact of [CCN] on drizzle formation.

Marine aerosols are mainly sulfur species, by mass. Nucleation mode aerosol particles are usually modeled as consisting of a solution of H_2SO_4 and $(NH_4)_2SO_4$. CCN particles are usually modeled as sea-salt particles and ammonium sulfate particles have grown, by condensation of vapor, from the nucleation mode particles. In this work, for simplicity, it will be assumed that H_2SO_4 is the only species both in the nucleation mode and the CCN mode particles. A bulk density of ρ_p=1.80 g cm^{-3} is used in this model (Seinfeld, 1986). Fig. 4.1 illustrates the physical process involved in this model.

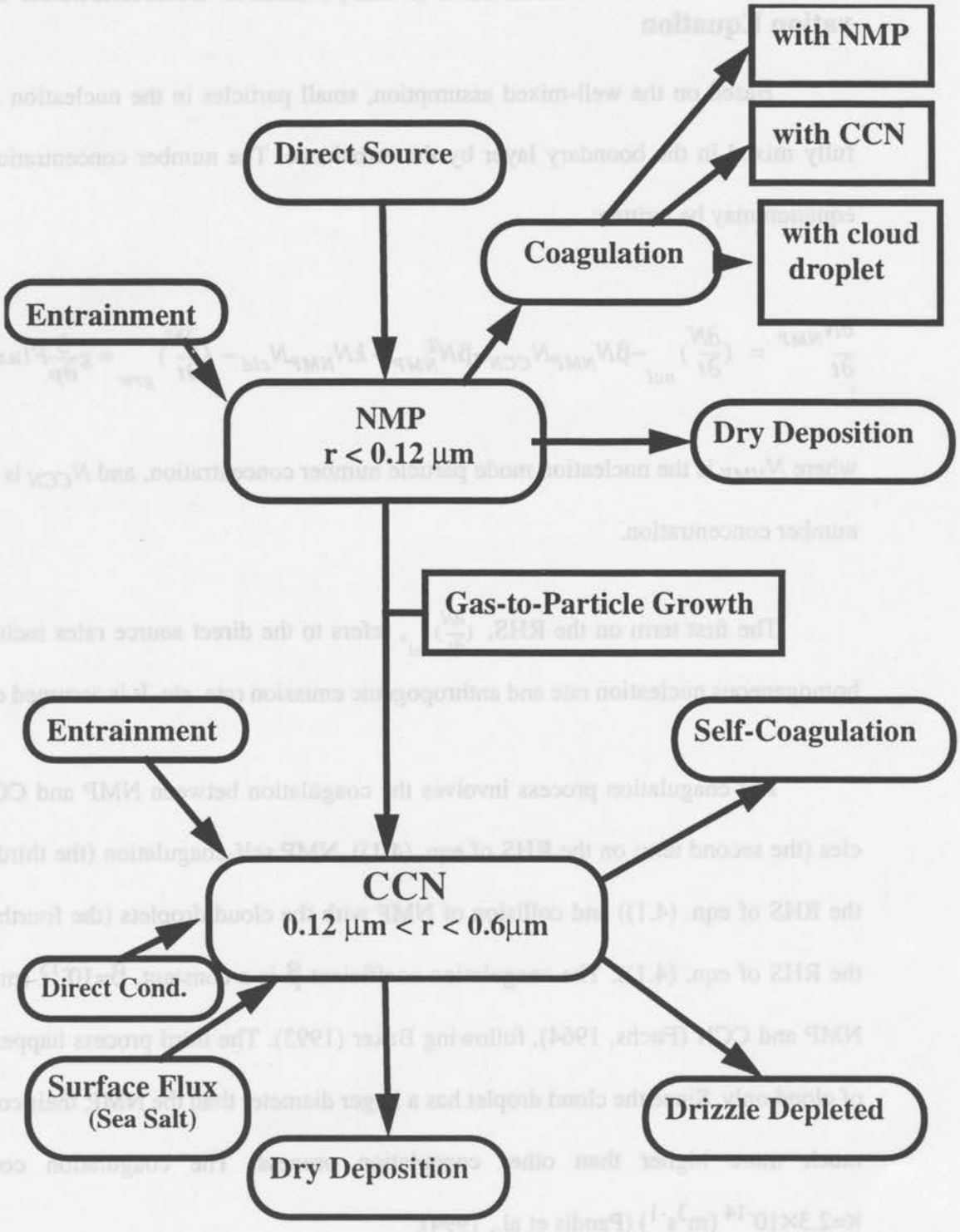

Fig. 4.1. A schematic diagram illustrates the aerosol and CCN physical processes.

4.2.1 Nucleation Mode Particles (NMP) Number Concentration Conservation Equation

Based on the well-mixed assumption, small particles in the nucleation mode are fully mixed in the boundary layer by the turbulence. The number concentration budget equation may be written:

$$\frac{\partial N_{NMP}}{\partial t} = \left(\frac{\partial N}{\partial t}\right)_{ncl} - \beta N_{NMP} N_{CCN} - \beta N_{NMP}^2 - k N_{NMP} N_{cld} - \left(\frac{\partial N}{\partial t}\right)_{grw} + g\frac{\partial}{\partial p} Flux_{N_{NMP}} \quad (4.1)$$

where N_{NMP} is the nucleation mode particle number concentration, and N_{CCN} is the CCN number concentration.

The first term on the RHS, $\left(\frac{\partial N}{\partial t}\right)_{ncl}$, refers to the direct source rates including the homogeneous nucleation rate and anthropogenic emission rate, etc. It is assumed constant.

The coagulation process involves the coagulation between NMP and CCN particles (the second term on the RHS of eqn. (4.1)), NMP self-coagulation (the third term on the RHS of eqn. (4.1)) and collision of NMP with the cloud droplets (the fourth term on the RHS of eqn. (4.1)). The coagulation coefficient β is a constant, $\beta=10^{-15}$ (m^3s^{-1}), for NMP and CCN (Fuchs, 1964), following Baker (1993). The third process happens inside of cloud only. Since the cloud droplet has a larger diameter than the NMP, their collision is much more higher than other coagulation process. The coagulation coefficient, $\kappa=2.3\times10^{-14}$ (m^3s^{-1}) (Pandis et al., 1994).

The fifth term on the RHS of Eqn. (4.1) is the condensational growth rate. Condensational growth is the main sink of nucleation mode particles below the cloud. Sulfuric

acid vapor condenses on the small particles growing them into the CCN mode. Following Pandis et al. (1994), the mass balance for the sulfuric acid gas-phase concentration is:

$$\frac{d[H_2SO_4]_g}{dt} = K_{SO_2}[OH]_g[SO_2]_g - \cancel{R_{nucl}}^{0} - (k_{mt1}N_{dry} + k_{mt2}N_{CCN})[H_2SO_4]_g$$

$$- k_{dep}[H_2SO_4]_g - R_{cloud}. \qquad (4.2)$$

The reaction constant for the SO_2 oxidation by the OH radical (Atkinson and Lloyd, 1984) is $K_{SO2} = 10^{-12}$ cm^3 molec^{-1} s^{-1}. The hydroxyl radical concentration is assumed to be $[OH]_g = 2\times10^6$ molec cm^{-3} (Crutzen and Zimmermann, 1991). The sulfur dioxide concentration is set to be 10 ppb for clean atmosphere (Seinfeld, 1986). Sulfate dioxide oxidation is the main gas-phase source of sulfuric acid in the MBL.

R_{nucl} is the homogeneous nucleation term. We assume it is negligible because of masses of the nuclei are very small and the nucleation rate is very small (Pandis et al, 1994).

The third term on the RHS of eqn. (4.2) represents the condensational loss. It includes both the condensation onto NMPs and that onto CCN. k_{mt1} and k_{mt2} are the sectional mass transfer coefficients which can be calculated by the integration of Fuchs-Sutugin equation.

The typical dry deposition velocity of H_2SO_4 is about 1 cm s^{-1} (Seinfeld, 1986). The dry deposition rate constant, k_{dep}, is 2×10^{-6} s^{-1} for a boundary layer height of 500 m.

The last term, R_{cloud} on the RHS of eqn. (4.2) refers to the loss of sulfuric acid by

condensation onto cloud droplets. Sulfuric acid vapor is scavenged by the cloud droplets in a very short time, so that R_{cloud} is very large. In this model, it is assumed that inside of cloud, sulfuric acid concentration is zero.

Therefore, the condensational growth rate of NMP inside of cloud is zero, $(\frac{\partial N}{\partial t})_{grwincld} = 0.$, and the condensational growth rate below cloud can be calculated using the chain rule (Pandis et al., 1994):

$$(\frac{\partial N}{\partial t})_{grw} = \frac{\partial N}{\partial m}\frac{\partial m}{\partial t} = kN_{NMP}[H_2SO_4]_g, \tag{4.3}$$

where $\frac{\partial N}{\partial m}$ refers to the mass chang rate when a NMP grows large enough to jump into the CCN bin. $\frac{\partial m}{\partial t} = k_{mtl}N_{NMP}[H_2SO_4]_g$ is the mass transfer rate of H_2SO_4 to NMP. Therefore, $k = \frac{\partial N}{\partial m} \bullet k_{mtl} = 1.52 \times 10^{-13}$ ppt^{-1} s^{-1} . [H_2SO_4] is the gas phase sulfate acid concentration. Assuming that sulfuric acid is in steady state in MBL, that is, $\frac{\partial}{\partial t}[H_2SO_4] = 0$, the steady state [$H_2SO_4$] can be obtained by solving eqn. (4.2) with the LHS equal to zero.

The last term in eqn. (4.1) refers to the turbulence transportation of NMP number concentration. Turbulence flux is a very important mechanism in keeping the NMP well-mixed throughout the whole boundary layer.

Integration of eqn. (4.1) through the whole boundary layer, using the well-mixed assumption, yields:

$$\frac{\partial N_{NMP}}{\partial t} = (\frac{\partial N}{\partial t})_{ncl} - \beta N_{NMP}N_{CCN} - \beta N_{NMP}^2 - kN_{NMP}N_{cld}\frac{P_c - P_{top}}{\Delta P_m}$$

$$-\left(\frac{\partial N}{\partial t}\right)_{grw}\frac{P_s - P_c}{\Delta P_m} + \frac{Flux_{NMPtop} + Flux_{sfc}}{\Delta P_m}, \tag{4.4}$$

where the first three terms on the right hand side of eqn. (4.4) are the same as that in eqn. (4.1) since the air is well-mixed. The fourth term is the NMP-cloud droplet collision process which has a contribution from the cloud layer only. The fifth term represents the condensational growth contribution below the cloud. The turbulence fluxes are expressed as the summation of the entrainment mass flux and the surface turbulent flux:

$$Flux_{NMPtop} = \frac{Eg}{\Delta P_m}(N_{NMPtop} - N_{NMP}), \tag{4.5}$$

and

$$Flux_{NMPsfc} = \rho C_{aero} V (N_{NMPsfc} - N_{NMP}), \tag{4.6}$$

where C_{aero} is the bulk aerosol coefficient in order to be in the same form like the aerodynamic coefficient.

If the boundary layer mean NMP number concentration is larger than that from above, the entrainment flux at the cloud top acts as a sink of N_{NMP}. Otherwise, the entrainment is a source of N_{NMP}. Since sea spray from the ocean is thought to carry primarily large sea salt particles. the surface dry particle concentration is assumed negligible, that is, N_{NMPsfc}=0. Thus, eqn. (4.5) actually represents the sedimentation of NMP to the surface, which is called the dry deposition process. Since C_{aero} is unknown, the calculation of eqn.(4.6) is uncertain. We will still use the formula for dry deposition in literature and set the dry deposition velocity, v_d = 0.04 cm s^{-1} (Pandis et al., 1994). Thus, the dry deposition process can be expressed as: $-\frac{\rho v_d}{\Delta P_m} N_{NMP}$.

Baker (1993) neglected both the top and surface turbulence flux, treating the whole boundary layer as an isolated box with no exchanges of chemical species in or out of the boundary layer by turbulence. However, Raes' model (1994) predicts that marine boundary layer-free atmosphere exchange by small scale turbulence at the cloud top affects the aerosol dynamics drastically. He also pointed out that this must be considered as a mechanism for CCN formation. The free atmosphere is a good source for small particles to the MBL, due to their long residence time of several weeks at higher altitudes.

4.2.2 CCN Number and Mass Concentration Budget

Similar to the treatment for NMP, it is assumed that the accumulation mode particles, which are the CCN are well-mixed within the boundary layer. Below cloud, CCN are not activated; inside of cloud, all of the CCN are assumed activated. Thus, the CCN number concentration equals the cloud droplet number concentration (Baker, 1993). The CCN number concentration budget is:

$$\frac{\partial N_{CCN}}{\partial t} = \left(\frac{\partial N}{\partial t}\right)_{grwblcld} + \left(\frac{\partial N}{\partial t}\right)_{grwincld} - \beta N_{CCN}^2 - \frac{g\rho_{air} V_t N_D}{\Delta P_m} + g\frac{\partial}{\partial p} Flux_{CCN}, \quad (4.7)$$

Following a similar derivation to that of NMP, After integration of eqn. (4.8), The CCN budget equation is obtained:

$$\frac{N_{CCN}}{t} = \left(\frac{\partial N}{\partial t}\right)_{grwblcld} \frac{P_s - P_c}{\Delta P_m} + \frac{gE}{\Delta P_m}(N_{CCNtop} - N_{CCN}) + \frac{\rho C_{aero} V}{\Delta P_m}(N_{sfc} - N_{CCN} - \beta N_{CCN}^2 - \frac{g\rho_{air} V_t N_D}{\Delta P_m}, \quad (4.8)$$

where N_{CCN} is the vertically integrated mean CCN number concentration. In the cloud layer, $N_{CCN} = N_{cld}$, the number concentration of cloud drops.

The condensational growth from nucleation mode particles below cloud is in a form exactly the same as that in Eqn. (4.4), except the condensational growth here is a source of CCN number concentration, while in Eqn.(4.4), it is a sink term.

Entrainment at the cloud top is another source of CCN number concentration. Since particles are able to survive in the free troposphere for several weeks, they have enough time to grow into accumulation mode particles by condensation and coagulation before they are engulfed into the MBL. However, if the boundary layer mean CCN number concentration is larger than that above the cloud top, the entrainment process will act as a sink of CCN number concentration. We may think of it as a diluting process to the MBL CCN in this situation.

Direct emissions from the ocean maybe a main source for CCN under some conditions. The turbulence at the ocean-air interface plays an important role in the transport of particles across the boundary. The surface turbulence term can be split into two parts:

$$\frac{\rho C_{aero} V}{\Delta P_m}(N_{sfc} - N_{CCN}) = \frac{\rho C_{aero} V}{\Delta P_m} N_{sfc} - \frac{\rho C_{aero} V}{\Delta P_m} N_{CCN}. \qquad (4.9)$$

The first term on the right hand side represents the emission rate of sea salt particles. The parameterization of Monahan et al. (1983) has been used to determine this source rate, where S_0 equals the first term in the RHS in eqn. (4.8):

$$S_0 = \frac{2.5 V^{3.41}}{z_t}, \qquad (4.10)$$

where V is the surface wind and z_t is the mixed layer height. The units of this flux rate are in particles $cm^{-3}day^{-1}$.

The second term on the RHS of eqn. (4.10) actually represents a loss of CCN number from the air, which is the dry deposition process. Since C_{aero} is unknown, we will still follow the same method in literature. Assuming the dry deposition velocity, v_d = 0.06 cm s^{-1}(Pandis et at., 1994), the dry deposition process can be expressed as: $-\frac{\rho v_d}{\Delta P_m} N_{CCN}$.

Coagulation among CCN particles may decrease the CCN number concentration and increase the droplet size. The coagulation coefficient, β, is assumed to be the same as that used in the NMP budget. The last term in eqn. (4.8) is the CCN particle removal process by drizzle. N_D represents the precipitable CCN number concentration.

Finally, we can rewrite eqn. (4.8) as:

$$\frac{\partial N_{CCN}}{\partial t} = \left(\frac{\partial N}{\partial t}\right)_{grwblcld} \frac{P_s - P_c}{\Delta P_m} + \frac{gE}{\Delta P_m}(N_{CCNtop} - N_{CCN}) + S_0 - \frac{\rho v_d}{\Delta P_m} N_{CCN} - \beta N_{CCN}^2 - \frac{g\rho_{air} V_t N_D}{\Delta P_m}. \tag{4.11}$$

Corresponding to the CCN number concentration, we may write a CCN mass balance equation as:

$$\frac{\partial M_{CCN}}{\partial t} = \left(\frac{\partial M}{\partial t}\right)_{grwbcld} \frac{P_s - P_c}{\Delta P_m} + \left(\frac{\partial M}{\partial t}\right)_{grwincld} \frac{P_c - P_b}{\Delta P_m} + \left(\frac{\partial M}{\partial t}\right)_{cond} \frac{P_s - P_c}{\Delta P_m} + \frac{gE}{\Delta P_m}(M_{CCNtop} - N_{CCN} m_{CCN}) + S_{m0} - \frac{\rho v_d N_{CCN} m_{CCN}}{\Delta P_m} - \frac{g\rho_{air} V_t N_D m_{CCN}}{\Delta P_m}, \tag{4.12}$$

where m_{CCN} is the individual CCN mass, which is calculated by: $m_{CCN}=M_{CCN}/N_{CCN}$. M_{CCNtop} is the CCN mass entrained with a fixed size of r=0.34 μm and S_{m0} is the direct

source rate of CCN mass with a fixed size of r=0.34 μm as well.

In eqn. (4.12), the second term represents the CCN mass condensational growth inside of the cloud by H_2SO_4 vapor. We assume that H_2SO_4 vapor goes into the cloud droplet right after it forms. Therefore, we have:

$$\left(\frac{\partial M}{\partial t}\right)_{grwincld} = k[OH]\,[SO_2]\,, \tag{4.13}$$

since the oxidation of SO_2 is the major source of H_2SO_4.

$\left(\frac{\partial M}{\partial t}\right)_{cond}$ in Eqn. (4.12) refers to the process of H_2SO_4 vapor condensation onto the existing CCN particles. It is in the form of:

$$\left(\frac{\partial M}{\partial t}\right)_{cond} = k_{mt2} N_{CCN} [H_2SO_4]\,. \tag{4.14}$$

Notice that the coagulation process is a removal mechanism for CCN number concentration only. It will not deplete the total CCN mass. Therefore, there is no coagulation term in eqn. (4.12).

Chapter 5

Model Results

The Atlantic Stratocumulus Transition Experiment (ASTEX) was conducted in June 1992 in the area near the Azores and Madeira Islands (28°-40°N, 16°-25°W) in the northeast Atlantic Ocean (Fig. 5.1). The main goal of ASTEX was to investigate the process by which stratus transitions to broken stratocumulus. Stratocumulus clouds tend to form over a cold ocean surface. The cloud layer might break up while moving over a warmer ocean surface (e.g. Klein and Hartmann, 1993). Since ASTEX was performed relatively far from the continental land masses, the air mass was more marine time than in FIRE (the First ISCCP (International Satellite Cloud Climatology Project) Regional Experiment) which was conducted near San Nicholas Island off the southern California coast. This is one motivation for choosing a case study from ASTEX to test the MBL model developed here.

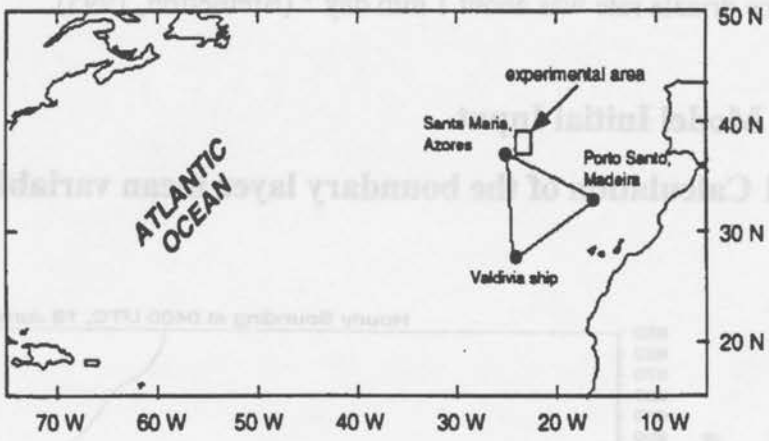

Fig. 5.1. ASTEX region on 12-13 June, 1992 (scanned from Duynkerke et al., 1995).

Two "Lagrangian" intensive observation experiments were conducted during ASTEX. ASTEX Lagrangian experiment one (L1) took place between 1600 UTC 12 June -1200 UTC 14 June in a clean marine air mass with low cloud droplet concentrations of 50-75 cm^{-3}. ASTEX Lagrangian experiment two (L2) was performed between 2200 UTC 18 June - 1400 UTC 20 June in an air mass that originated in continental Europe, with a cloud droplet number concentration of 200-300 cm^{-3} (Bretherton, 1995). In L1, a steady stratocumulus cloud existed and drizzle was frequently observed on all near surface aircraft flight legs (pressures above 1000 mb). In L2, the stratocumulus cloud was broken up, cumulus clouds were observed under the stratocumulus, and less drizzle was observed.

This report focuses on the drizzle parameterization. Therefore, data from ASTEX Lagrangian 1 was used and simulated. Since the model does not currently include solar radiation, the night-time data is used. The simulation period to be presented is from 2000 UTC 12 June to 0800 UTC 13 June. During most of this time, the SST is colder than the

air surface temperature. Drizzle reached the surface frequently and the estimated average surface drizzle rate was about 1 mm day^{-1} (Bretherton, 1995).

5.1. Model Initial Input

5.1.1 Calculation of the boundary layer mean variables

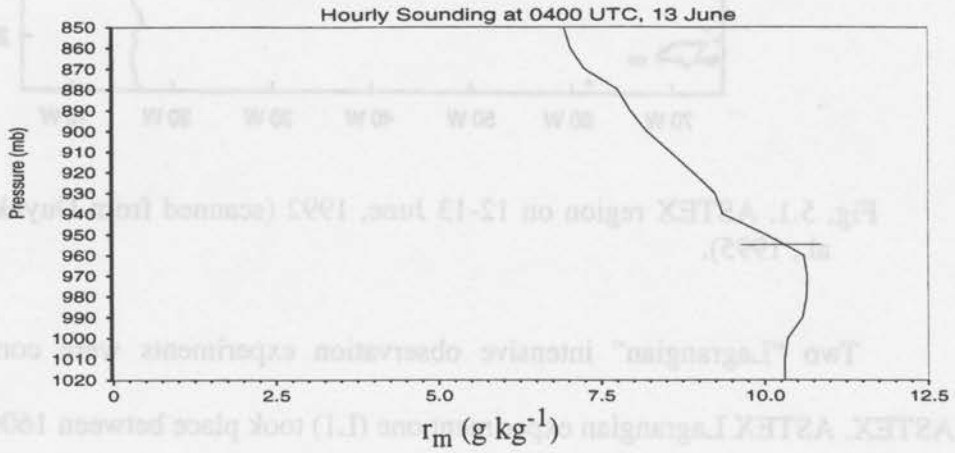

Fig. 5.2. Blended composite hourly sounding of the total water mixing ratio (r_m) at 0400 UTC, 13 June. The horizontal bar indicates the observed boundary layer top. (Data from ASTEX www)

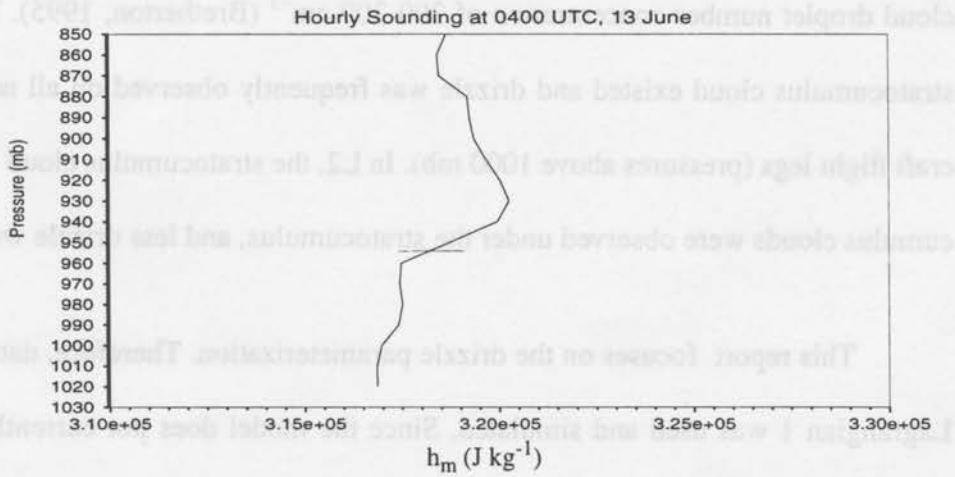

Fig. 5.3. Blended composite hourly sounding of the mean moist static energy (h_m) at 0400 UTC, 13 June. The horizontal bar indicates the observed boundary layer top. (Data from ASTEX www)

Fig. 5.2 and Fig. 5.3 show the hourly soundings of total water mixing ratio and moist static energy at 0400 UTC, 13 June. The soundings do not show a sharp decrease or increase at the boundary layer top. The values used for the boundary layer top condition depend on the location of the boundary layer top, and the average values depend on the depth of the layer which is averaged. In Chapter 6, some model sensitivity studies using different boundary layer top conditions will be shown.

The total water mixing ratio, moist static energy, wind and equivalent potential temperature are assumed to be constant with height in the mixed layer. Using this assumption and averaging the hourly sounding data below the boundary layer top, around 960 mb, one can obtain the well-mixed layer mean total mixing ratio (r_m), mean moist static energy (h_m), and mean wind speed (v_m). The boundary layer top thermodynamic conditions r_{top}, h_{top}, and v_{top}, are calculated by averaging the sounding data in a layer 20 mb to 50 mb thick above the cloud top, e.g.,

$$S_{top} = \frac{1}{\sum k} \bullet \sum_{k=P_{low}}^{P_{high}} S_i,$$

where S refers to an arbitrary variable; k refers to the vertical levels; P_{high} is the upper level limit and P_{low} is the lower level limit. Thus, the boundary top jump condition is:

$$\Delta S = S_{top} - S_m,$$

where S_m refers to any mean boundary layer variable.

Table 5.1 is a summary of the methods using in the calculation of the thermodynamic conditions in this model.

Table 5.1: The calculation of the thermodynamic conditions.

Top P_{high} (mb)	Top P_{low} (mb)	r_m (kg kg^{-1})	h_m (J kg^{-1})	wind (m s^{-1})
P_i-50 mb	P_i-20 mb	Average Below P_i	Average Below P_i	Average Below P_i

5.1.2 The initial run and the control run

The method used for the simulations is as follows:

We input the observational data at 2000 UTC as the initial condition and set the initial $[N_{CCN}]_m$ = 100 cm^{-3}, $[N_{CCN}]_{top}$ = 200 cm^{-3} and TKE = 0.155 m^{2}s^{-2}. We fixed all of the initial conditions except the TKE and run the model for two hours to let the TKE equilibrate. Then, we restart all of the initial conditions except the turbulence kinetic energy.

The interpolated hourly data for the SST, surface pressure, large-scale divergence, boundary top conditions (r_{top}, h_{top}, etc.) and longwave radiative cooling rate are used as the input at each time step. The model is run for a total time of twelve simulated hours, excluding the first two hours of initial warm-up.

5.2. Boundary Layer Depth

Fig. 5.4 shows the simulated boundary layer top position from 2000 UTC, 12 June to 0800 UTC, 13 June. The local time is one hour earlier than UTC, that is, 7:00 p.m., 12 June to 7:00 a.m., 13 June. The model prediction is in good agreement with the observed. The maximum error is only about 8 mb.

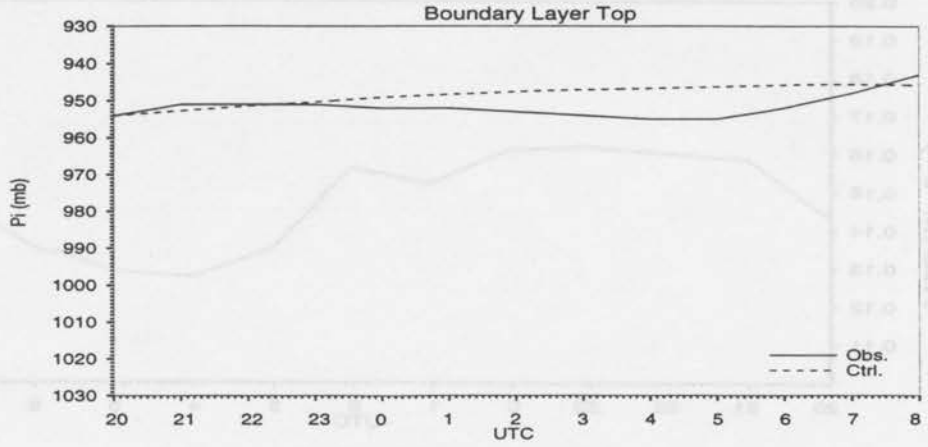

Fig. 5.4. Evolution of the boundary layer depth. x-axis represents the universal time (UTC). Unit: hour. y-axis denotes the boundary layer height. Unit: mb. Solid line represents the observation. Dashed line the control run.

The boundary layer depth determines the total boundary layer mass. The boundary layer mass budget is a balance between the large-scale divergence and the entrainment mass flux. The observed larger-scale divergence is almost constant, about 5×10^{-6} s^{-1}, during the simulation time period. Thus, the boundary layer becomes shallower or deeper depending on whether the entrainment flux from the cloud top is stronger or weaker than the large-scale divergence.

5.3. Turbulence Kinetic Energy and the Entrainment Mass Flux

The evolution of the vertically integrated mean TKE is shown in Fig. 5.5. There is a tendency for a diurnal variation in the TKE as well. Although the diurnal variation is not explicitly represented in the model, the model's inputs at each time step such as observed SST, surface pressure and mean wind, already contain information about the diurnal variation.

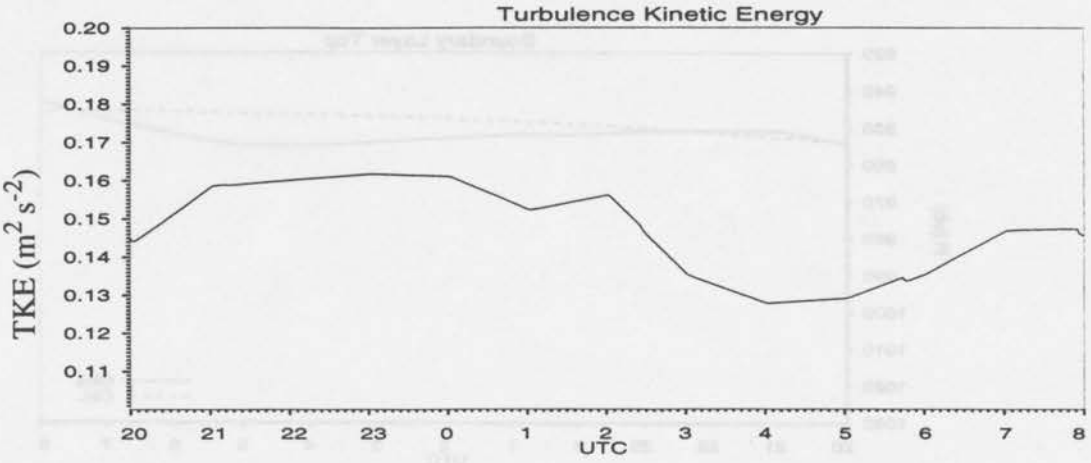

Fig. 5.5. Evolution of the turbulence kinetic energy from model. x-axis represents the universal time. Unit: hour. y-axis denotes the TKE. Unit: $m^2 s^{-2}$.

Corresponding to the turbulence kinetic energy, Fig. 5.6 shows the variation of entrainment mass flux with time. Entrainment mass flux is approximately proportional to the square-root of TKE. Entrainment mass flux equals $\rho_{air} w_e$, where w_e is the entrainment velocity. w_e was estimated to be within 0.1 cm s^{-1} to 1.1 cm s^{-1} for the whole period of L1 (Bretherton, 1995). Assuming ρ_{air}=1.275 kg m^{-3}, the modeled entrainment velocity is between 0.2 cm s^{-1} to 0.6 cm s^{-1}, in reasonable agreement with Bretherton (1995) estimate.

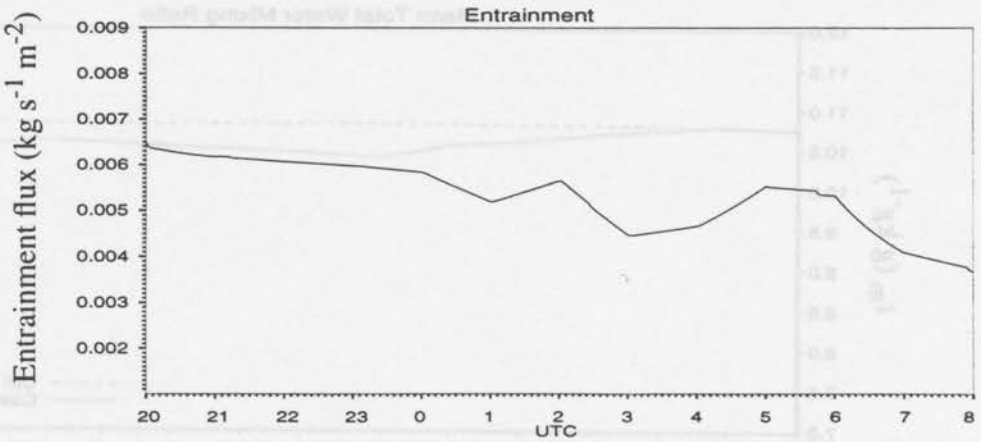

Fig. 5.6. The model entrainment mass flux versus time. x-axis represents the universal time. Unit: hour. y-axis represents the entrainment mass flux. Unit: kg s^{-1} m^{-2}.

5.4. Mean Total Water Mixing Ratio and Mean Moist Static Energy

As shown in Figure 5.7, the model predicts a wetter boundary layer than observed, although the error is less than 5%. Possible explanation are that the prescribed free atmosphere is too wet, or that the predicted precipitation rate is too small. The sensitivity to the jump condition will be shown in the next chapter. The vertically integrated mean moist static energy is shown in Fig. 5.8. The model predicts the boundary layer energy fairly well with a maximum error of only about 1%.

Both the total water mixing ratio and the moist static energy are observed to reach their minimum at about 1:00 a.m. local time, as shown in the observation. However, the model does not reproduce this minimum.

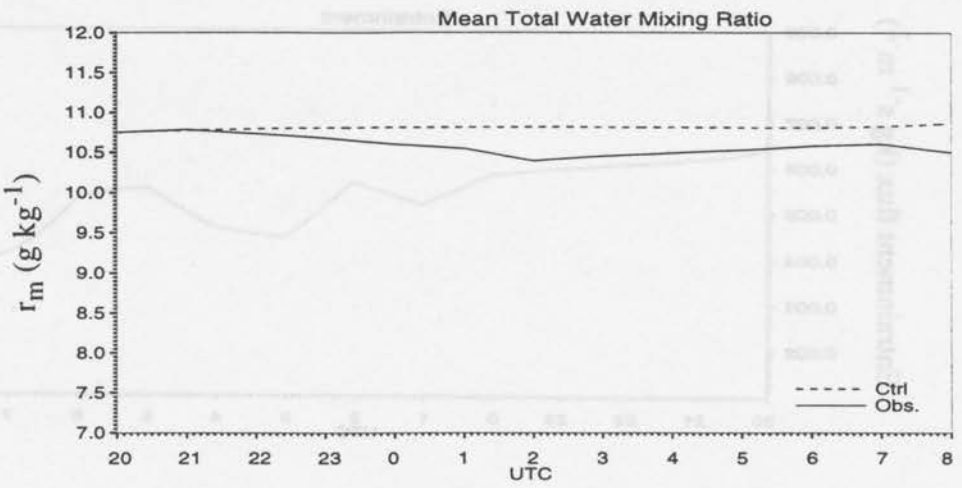

Fig. 5.7. Evolution of the total water mixing ratio. x-axis represents the universal time. Unit: hour. y-axis represents the mean mixing ratio (r_m). Unit: g kg^{-1}.

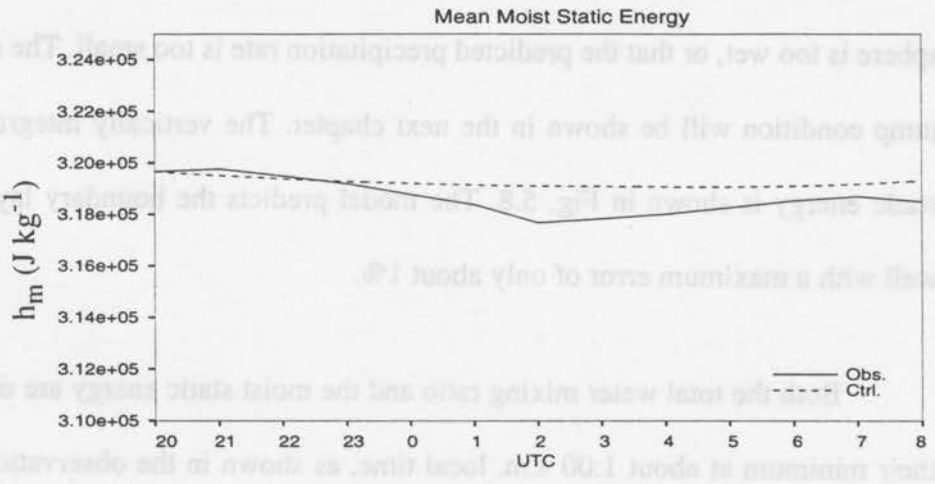

Fig. 5.8. Evolution of the mean moist static energy. x-axis represents the universal time. Unit: hour. y-axis represents the mean moist static energy (h_m). Unit: J kg^{-1}.

5.5. Cloud and Drizzle

5.5.1 Cloud thickness and cloud water

During the first day of ASTEX L1, the marine boundary layer was capped by a solid, drizzling stratocumulus cloud layer (Bretherton and Pincus, 1995). The model predicts a night time cloud about 350 m thick (Fig. 5.9).

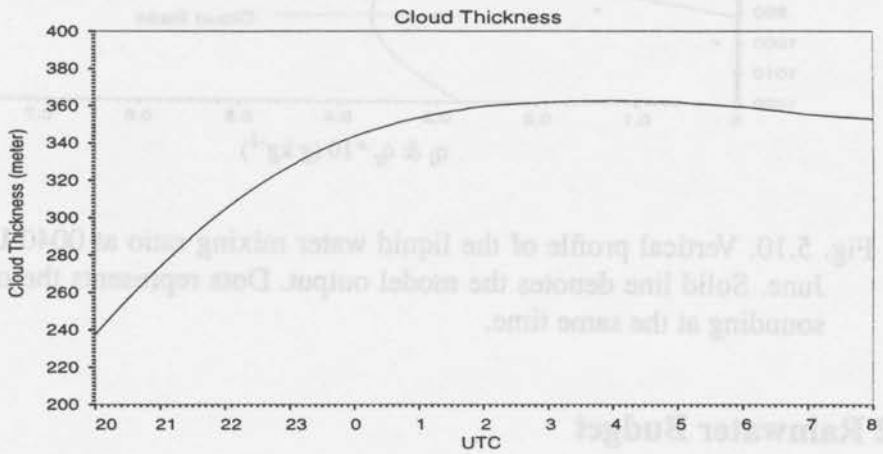

Fig. 5.9. The evolution of the cloud thickness between 2000 UTC, 12 June to 0800 UTC, 13 June. Unit: meter.

The liquid water content is almost linear with height in the cloud layer (Fig. 5.10). The liquid water mixing ratio reaches its maximum near the cloud top and dramatically decreases above the cloud top. Below cloud, the liquid water mixing ratio is zero because the air is unsaturated. At 0400 UTC, the boundary layer cloud is fully developed and about 360 m thick (Fig. 5.9). The maximum liquid water reaches 0.73 g kg^{-1} near the cloud top. The rainwater mixing ratio is one order of magnitude smaller than the cloud water mixing ratio. The rainwater mixing ratio reaches its maximum of about 0.036 g kg^{-1} near the cloud base. Below the cloud layer, rainwater decreases towards the sea surface due to

evaporation.

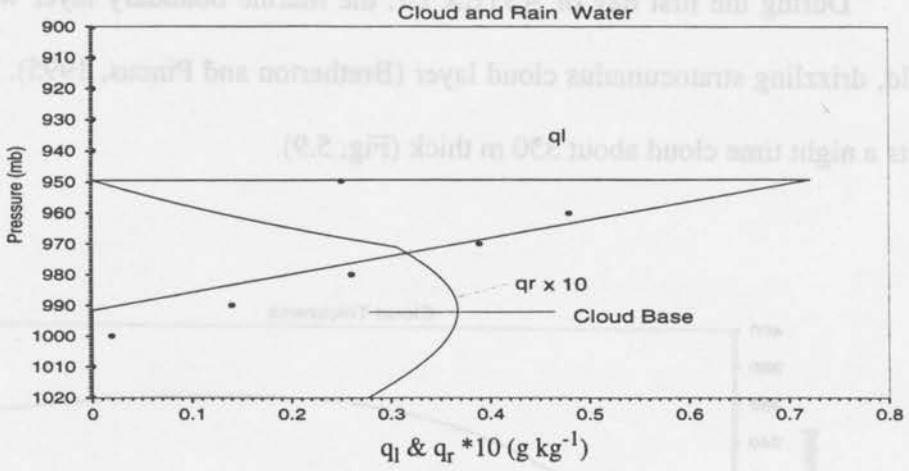

Fig. 5.10. Vertical profile of the liquid water mixing ratio at 0040 UTC, 13 June. Solid line denotes the model output. Dots represents the observed sounding at the same time.

5.5.2 Rainwater Budget

The rainwater budget is shown in Fig. 5.11. In the cloud layer, the autoconversion turns the cloud water into rainwater. Rainwater further collects the cloud water by the accretion process. These two processes are the sources of rainwater. The drizzle flux diverges and tries to remove the rainwater from the cloud layer. It is a sink of rainwater inside cloud. The maximum autoconversion rate (about 10.7 g kg^{-1} day^{-1}) occurs near the cloud top due to the highest cloud water content at that level. The maximum divergence of the drizzle gravitational flux also occurs near the cloud top. Below cloud base, rainwater is depleted by evaporation. This is balanced by the convergence of the drizzle gravitational flux. As to the total water mixing ratio ($q_l + q_v$), in order to keep it constant with height, the turbulent moisture flux varies and tries to balance the drizzle effects.

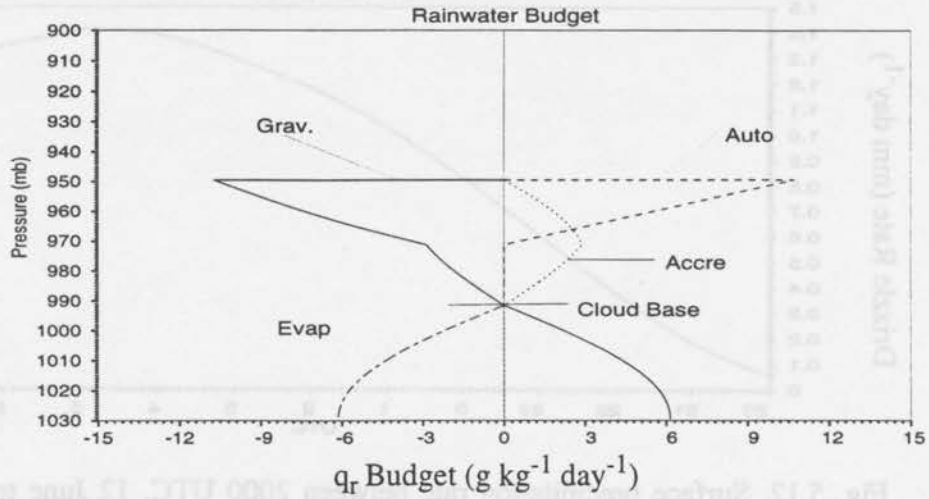

Fig. 5.11. Rainwater budget at 0400 UTC, 13 June. Solid line represents the divergence of the drizzle gravitational flux (Grav.); dashed line, the auto conversion rate (Auto); dotted line, the Accretion rate (Accre); dot-Dashed line, the evaporation rate. Unit: g kg^{-1}day^{-1}. Horizontal bar denotes the cloud base position.

5.5.3 Precipitation Rate

Drizzle reached the sea surface frequently during ASTEX L1. It was reported that the mean drizzle rate over this period was about 1 mm day^{-1}(Bretherton, 1995). The model shows an increase of the surface drizzle rate during the simulation. The highest simulated drizzle rate is about 1.4 mm day^{-1} around 0400 -0500 UTC, 13 June (Fig. 5.11). During this period, the cloud layer is the thickest as well. Since there are no direct surface observations to compare with, a series of vertical profiles of drizzle flux during 0200 - 0600 UTC based on aircraft data from the Electra and the C130 are shown in Fig. 5.12. The model simulations are in reasonable agreement with the observations.

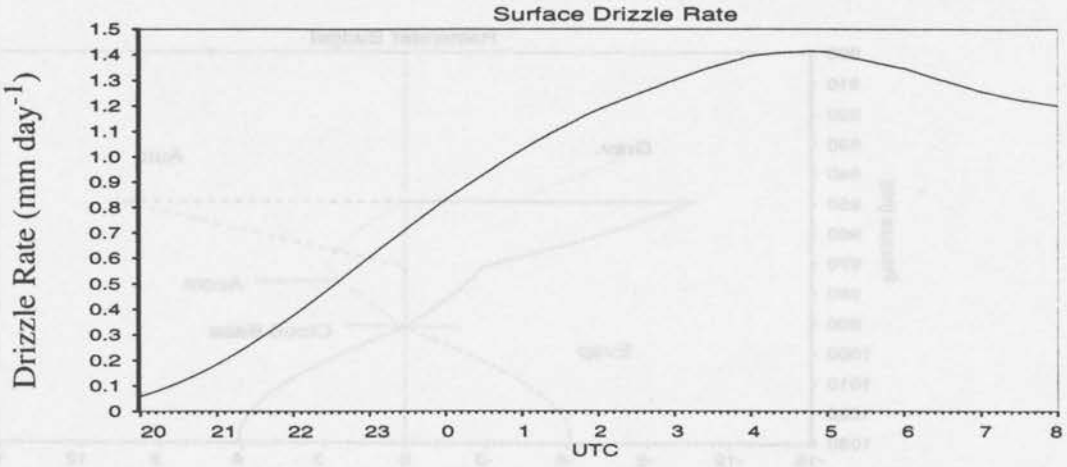

Fig. 5.12. Surface precipitation rate between 2000 UTC, 12 June to 0800 UTC, 13 June. Unit: mm day^{-1}.

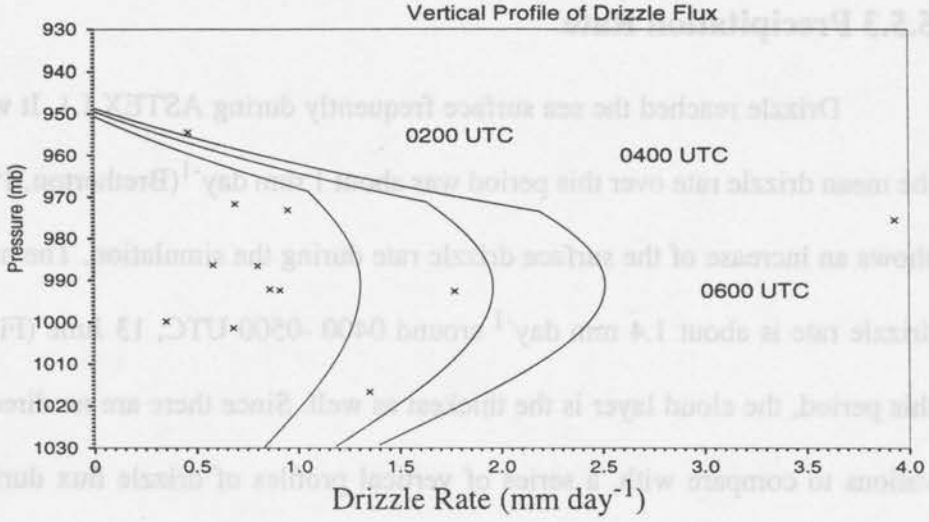

Fig. 5.13. Vertical profiles of drizzle flux. Solid lines represents the model output at 0200 UTC, 0400 UTC and 0600 UTC, respectively. The cross points represents the aircraft data during this 4-hour period (from ASTEX www)

5.5.4 Drizzle droplet sizes

The drizzle droplets are assumed to follow the Marshall-Palmer distribution. The rain drops are small at the cloud top since rain water concentration is low at that level. The mean radius reaches its maximum of about 90 μm at the cloud base. Below the cloud layer, the drizzle size slightly decreases due to evaporation. Chen and Cotton (1987) pointed out that the mean drizzle radius for stratocumulus clouds varies from 40 μm to 270 μm. The simulation is within this range.

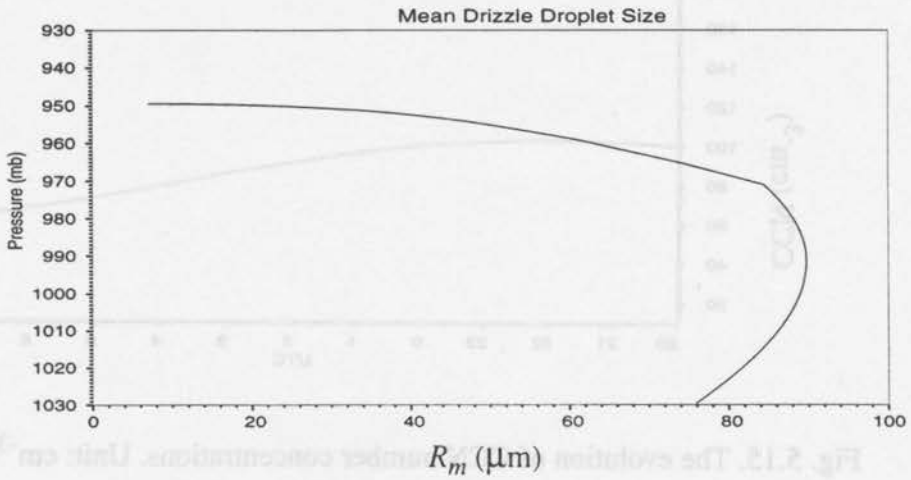

Fig. 5.14. Vertical profiles of mean drizzle size. x-axis represents the mean radius. Unit: μm. y-axis the pressure scale.

5.6. Cloud Condensation Nuclei (CCN)

ASTEX L1 focused on a clean marine air mass with an average cloud droplet number concentration of about 100 cm^{-3} (ASTEX data from world wide web). Since there are no direct source and sink measurements for the CCN number concentration in ASTEX, the simulations for CCN formation and depletion in this thesis are based on previous work by others. The main goal here is not to estimate the CCN number concentration, for which

there are no good observational data, but to study how the variation of CCN affects the boundary layer properties. This will be discussed further in Chapter 6. Fig. 5.15 shows the evolution of CCN number concentration during control run. In this simulation, the air above the boundary layer was assumed to contain 200 cm^{-3} CCN which could be entrained into the MBL. The model predicted CCN number concentrations are within 50 to 110 cm^{-3}.

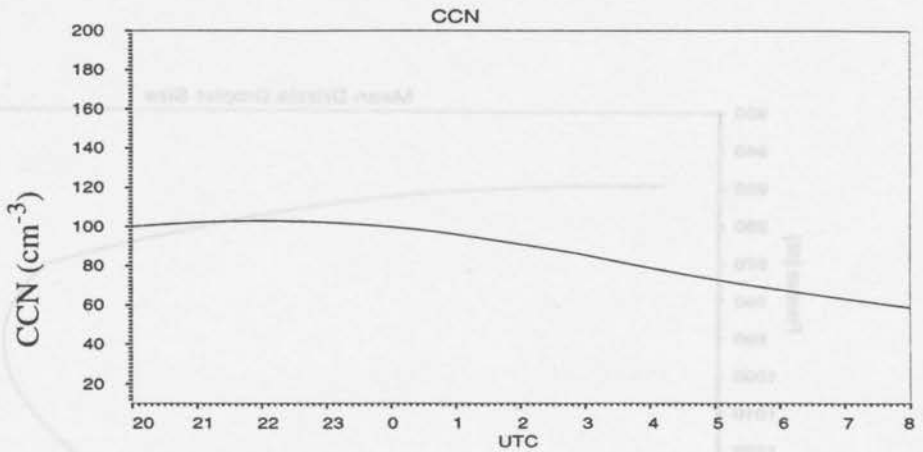

Fig. 5.15. The evolution of CCN number concentrations. Unit: cm^{-3}.

Each CCN production rate is shown in Fig. 5.16. Entrainment and the direct source rate are the two major sources while precipitation removal is the major sink of CCN number concentrations. As the drizzle reaches its maximum around 0500 UTC, June 13, the drizzle removal reaches its maximum rate of about 1700 m^{-3} s^{-1}.

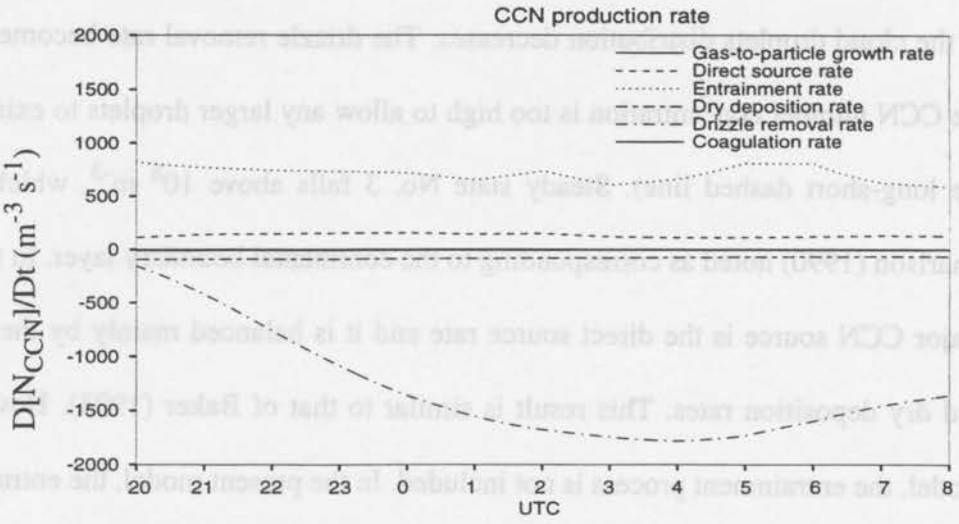

Fig. 5.16. The CCN production rate as a function of time. Unit: m^{-3} s^{-1}.

Since the marine boundary layer CCN number concentration is usually not very variable, attention has often been focused on steady state studies of CCN. The steady state solutions of CCN number concentrations, for fixed thermodynamic boundary layer conditions, are shown in Fig. 5.17, which is constructed after a simple figure in Baker and Charlson (1990). Two stable steady states are obtained (marked as No. 1 and No. 3). Steady state No. 1 is in the range from 10^7 - 10^8 m^{-3}, which corresponds to a drizzling marine boundary layer. In this case, the main CCN source rates are the entrainment and the direct source rates, and these are balanced by the precipitation sink (Fig. 5.18). The response of the drizzle removal to the [CCN] is similar to that discussed in Section 3.7 for a fixed liquid water mixing ratio. Drizzle removal increases when [CCN] increases while the CCN number concentrations are low, since increasing [CCN] increases the number concentration of particles in the larger-particle fraction. When the CCN number concentrations are high, the drizzle removal rate decreases when [CCN] increases. That is

because the liquid water is not sufficient to allow many larger droplets, the mean diameter of the cloud droplets distribution decreases. The drizzle removal rate becomes zero when the CCN number concentration is too high to allow any larger droplets to exist (Fig. 5.18, the long-short dashed line). Steady state No. 3 falls above 10^8 m^{-3}, which Baker and Charlson (1990) noted as corresponding to the continental boundary layer. In this case, the major CCN source is the direct source rate and it is balanced mainly by the coagulation and dry deposition rates. This result is similar to that of Baker (1993). However, in her model, the entrainment process is not included. In the present model, the entrainment from the free atmosphere, for which $[CCN]_{top}$ = 200 cm^{-3} has been assumed, acts as a significant source of CCN when the free atmosphere air mass is relatively "dirty", while it acts as a sink when the free atmosphere air mass is relatively clean (Fig. 5.17, the dotted line).

Steady state No. 2 is an unstable state. If a small perturbation of either an increase or a decrease in the CCN number concentration is applied to this steady state, the steady state will be totally destroyed. However, for the other two steady states, a small increase in the CCN number concentrations will make DN/Dt negative so that the CCN number concentrations decrease and go back to the steady state, while a small decrease in the CCN number concentrations will make DN/Dt positive so that the CCN number concentration increases and is forced back to the steady state.

As in Baker's (1993) paper, there is a sharp discontinuity between the two steady states. In her model, the critical radius drizzle threshold was fixed at r_{cr} = 10 μm. The sharp discontinuity occurs at that CCN number concentration which satisfies r_{cr} = 10 μm at a fixed cloud water mixing ratio. In this model, since the drizzle rate is controlled by the

CCN number concentration, a smoother region exists between the two steady states. This supports the idea that there is no sharp transition between the drizzle and non-drizzle steady states in the marine boundary layer (Gerber, in press).

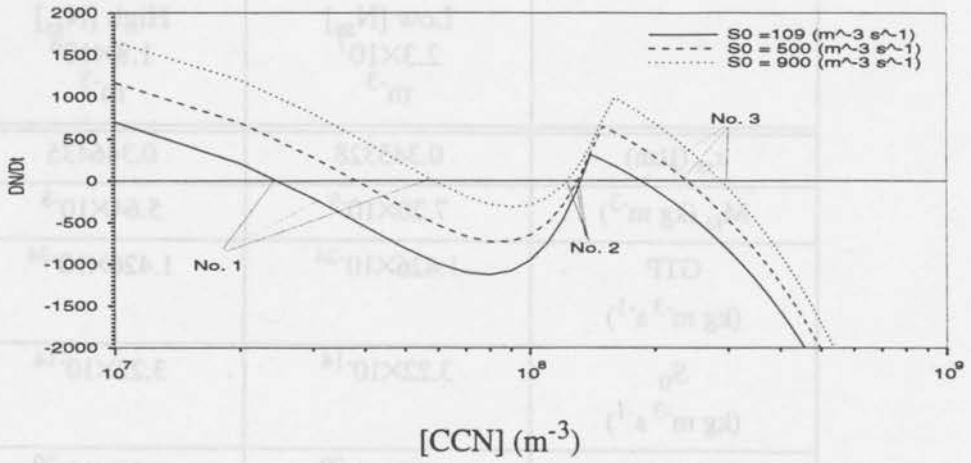

Fig. 5.17. The rate of change of CCN number concentration N, as a function of CCN number concentration, for three different direct source rates, S_0.

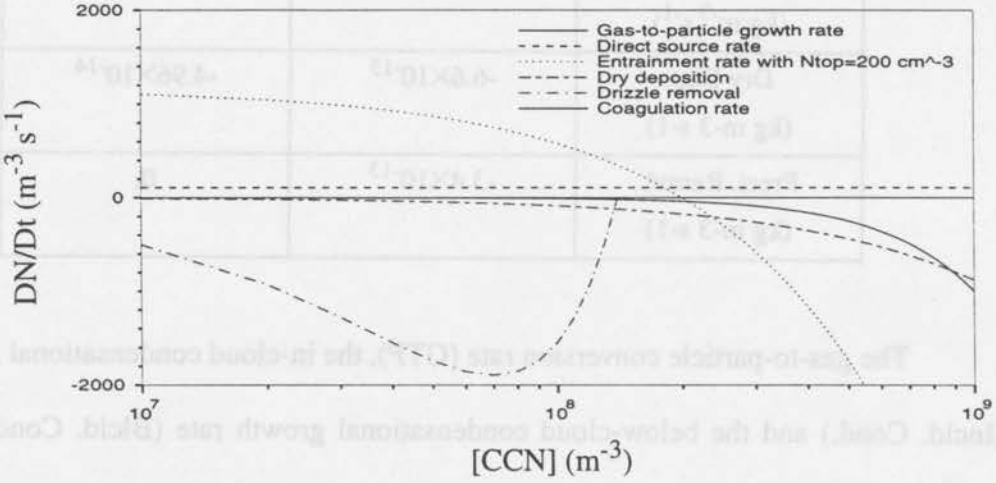

Fig. 5.18. Each production rate of CCN number concentration as a function of [CCN] for the control run.

In this model, a CCN mass budget is coupled with the number concentration

budget. As shown in Table 5.2, for both stable steady states, the mass mean CCN sizes (r_{ss}) do not change much from the initial condition, r_m = 0.34 μm.

Table 5.2: CCN Mass Budget for the Two Stable Steady States

	Low [N_{ss}] 2.3×10^{7} m^{-3}	High [N_{ss}] 1.8×10^{8} m^{-3}
r_{ss} (μm)	0.345328	0.346435
M_{ss} (kg m^{-3})	7.20×10^{-9}	5.64×10^{-8}
GTP (kg m^{-3} s^{-1})	1.426×10^{-24}	1.426×10^{-24}
S_0 (kg m^{-3} s^{-1})	3.22×10^{-14}	3.22×10^{-14}
Incld. Cond. (kg m^{-3} s^{-1})	4.25×10^{-20}	4.25×10^{-20}
Blcld. Cond. (kg m^{-3} s^{-1})	8.71×10^{-21}	6.81×10^{-20}
Entrainment (kg m^{-3} s^{-1})	2.99×10^{-13}	1.60×10^{-14}
Dry Dep. (kg m-3 s-1)	-6.6×10^{-15}	-4.96×10^{-14}
Preci. Remvl. (kg m-3 s-1)	-3.4×10^{-13}	0.

The gas-to-particle conversion rate (GTP), the in-cloud condensational growth rate (Incld. Cond.) and the below-cloud condensational growth rate (Blcld. Cond.) are very small compared with the other rates, and are negligible. For the lower [N_{ss}], the steady state mass is balanced mainly among the direct source rate (S_0), the entrainment rate and the precipitation removal. In contrast, for the higher [N_{ss}], the steady state mass is mainly

a balance among the direct source rate, the entrainment rate and the dry deposition rate, since in this case the precipitation rate is zero. This mass balance is different from the number concentration balance. In the CCN number concentration balance, the coagulation process is a major sink for the higher [N_{ss}], but coagulation is not a mass removal mechanism and thus does not play a role in the steady state mass balance.

Chapter 6

Sensitivity Studies

6.1. Sensitivity to the Boundary Layer Top Jump Conditions

As discussed in the previous chapters, the diagnosed of the boundary layer top thermodynamic jump condition depends on both the boundary layer top position and the depth of the layer above the BL top over which the variable is averaged. Thus, the model is tested for three different cases (Table 6.1). In Run 1, r_{top} is decreased by 20% and the other boundary layer top variables are fixed as the control run. In Run 2, the boundary layer top moist static energy is decreased by about 10% and the mixing ratio is fixed.

Table 6.1: Sensitivity Test to the Jump Conditions

Ctrl. Run	Run 1	Run 2
r_{top}	$80\%*r_{top}$	r_{top}
h_{top}	h_{top}	$110\%*h_{top}$

Fig. 6.1 shows the sensitivity of the total water mixing ratio to the jump conditions. As the free troposphere is made drier, the whole boundary layer becomes drier (dotted line) due to the entrainment of dry air from the boundary layer top. The model output for Run 1 is in better agreement with the observations than is the control run. Since the boundary layer is drier, the mean moist static energy decreases. The moist static energy flux, F_h, and the moisture flux, F_r, increase (eqn. 3.12). This makes the buoyancy production larger so that the boundary layer become more turbulent, and thus the boundary layer grows deeper (Fig. 6.2).

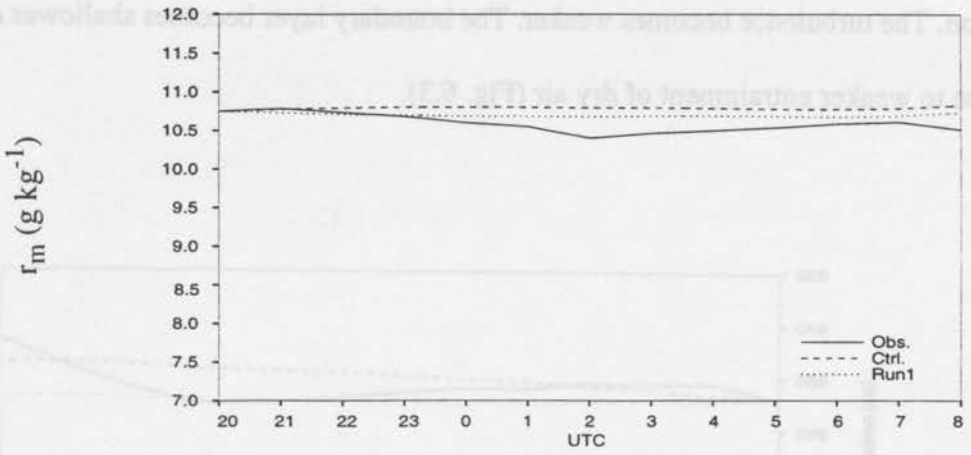

Fig. 6.1. Sensitivity tests of total water mixing ratio on different boundary layer top mixing ratio, r_{top}. Solid line represents the observations. Dashed line the control run. Dotted line, Run 1, decreasing the r_{top} to its 80%.

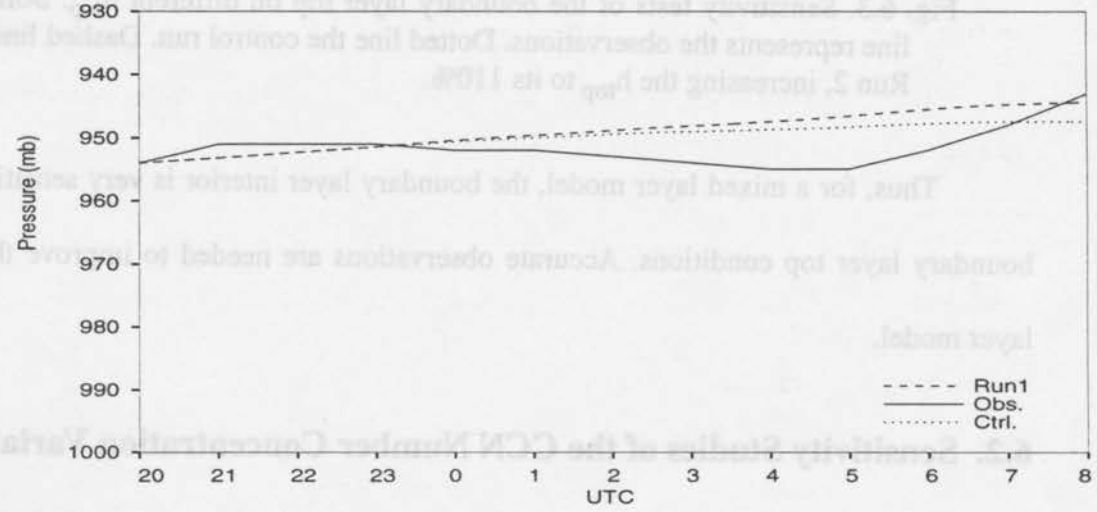

Fig. 6.2. Sensitivity tests of the boundary layer top on different r_{top}. Solid line represents the observations. Dotted line the control run. Dashed line, Run1, decreasing the r_{top} to its 80%.

Similarly, if the boundary layer top moist static energy increases by 10% which is about 1K warmer than the control run, the mean moist static energy in the boundary layer

will increase. The moist static energy flux decreases and this leads to a less buoyancy production. The turbulence becomes weaker. The boundary layer becomes shallower and wetter due to weaker entrainment of dry air (Fig. 6.3).

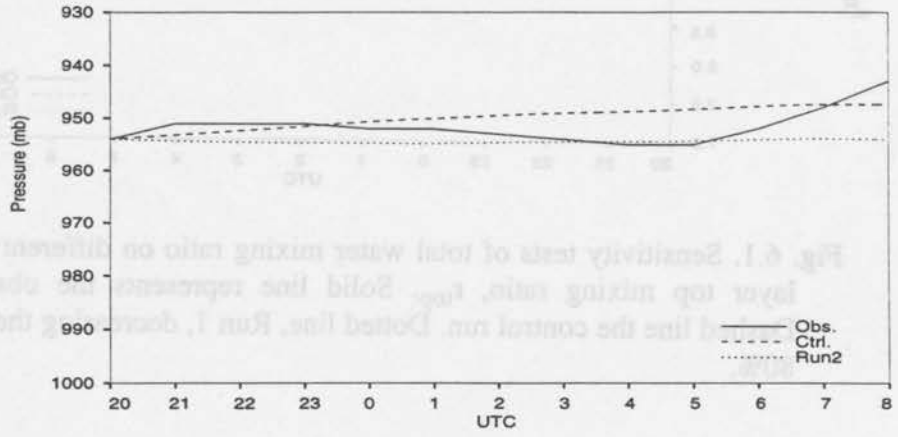

Fig. 6.3. Sensitivity tests of the boundary layer top on different h_{top}. Solid line represents the observations. Dotted line the control run. Dashed line, Run 2, increasing the h_{top} to its 110%.

Thus, for a mixed layer model, the boundary layer interior is very sensitive to the boundary layer top conditions. Accurate observations are needed to improve the mixed layer model.

6.2. Sensitivity Studies of the CCN Number Concentration Variation

Although the cloud droplet number concentration in the stratocumulus cloud layer over the marine boundary layer generally lacks extreme variability, it has been shown that a small changes in the droplet number concentration can have important impacts on the cloud radiative properties (Slingo,1990).

Three case studies are shown in Table 6.2. In the control run, an initial condition of

[CCN]=100 cm^{-3} is given and the free atmosphere CCN number concentration is assumed to be $[CCN]_{top}$ = 200 cm^{-3}. In Run 3, the CCN number concentration is fixed through the whole model. In Run 4, the initial condition of CCN number concentration is the same as that in the control run, while the free atmosphere CCN number concentration decreases to $[CCN]_{top}$ = 100 cm^{-3}.

Table 6.2: Sensitivity studies of the CCN effect on BL

Ctrl. Run	Run3	Run4
Ini. Cond. $[CCN]_m$=100 cm^{-3}	Fix [CCN]=100 cm^{-3}	Ini. Cond.$[CCN]_{top}$=100 cm^{-3}
$[CCN]_{top}$ =200 cm^{-3}	----------	$[CCN]_{top}$ =100 cm^{-3}

The evolution of the CCN number concentration is shown in Fig. 6.4. Although CCN number concentration varies with different cases, it varies within the same order of magnitude. This range is within the typical CCN number concentration for the marine boundary layer, 10-200 cm^{-3}.

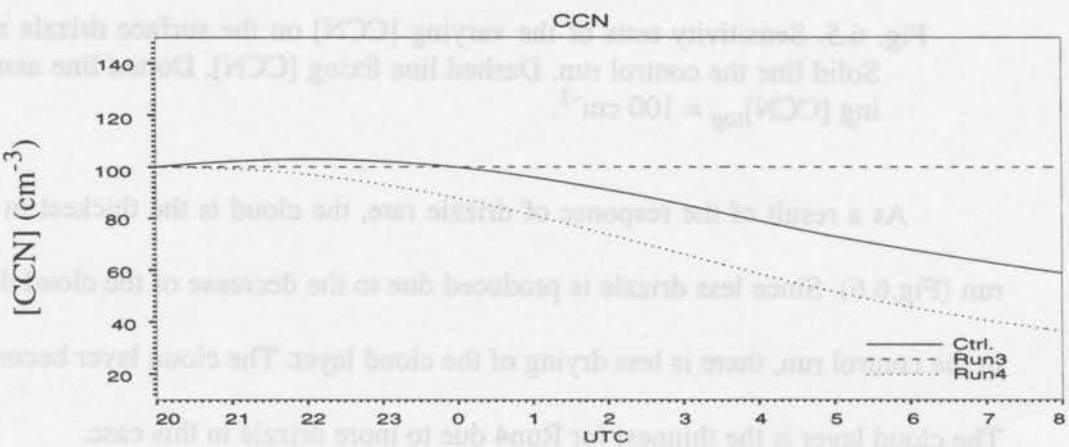

Fig. 6.4. The evolution of [CCN] for three different cases. Solid line is the control run. Dashed line run fixing [CCN]= 100 cm^{-3}. Dotted line $[CCN]_{top}$=100 cm^{-3}.

For the highest CCN number concentration, Run 3, the surface drizzle rate is the lowest (Fig. 6.5). An increase in the CCN number concentration results in a decrease of the cloud droplet sizes. Fewer cloud droplets are able to pass the coalescence threshold of r_{cr} = 19 μm. Therefore, less drizzle is produced. For the lowest CCN number concentrations in Run 4, the surface drizzle rate is the highest. This is because a decrease in the CCN number concentration causes an increase of the cloud droplet sizes. Thus, there will be more cloud droplets passing the coalescence threshold to become raindrops.

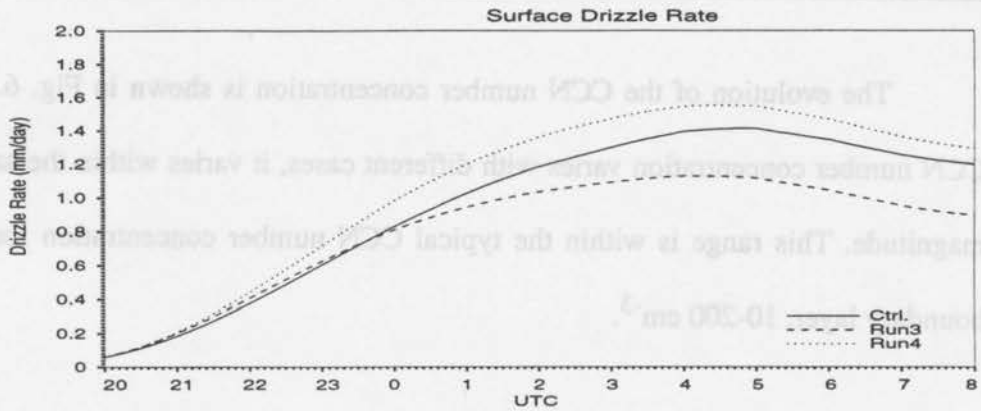

Fig. 6.5. Sensitivity tests of the varying [CCN] on the surface drizzle rate. Solid line the control run. Dashed line fixing [CCN]. Dotted line assuming $[CCN]_{top}$ = 100 cm^{-3}.

As a result of the response of drizzle rate, the cloud is the thickest in the control run (Fig.6.6). Since less drizzle is produced due to the decrease of the cloud droplet sizes in the control run, there is less drying of the cloud layer. The cloud layer becomes thicker. The cloud layer is the thinnest for Run4 due to more drizzle in this case.

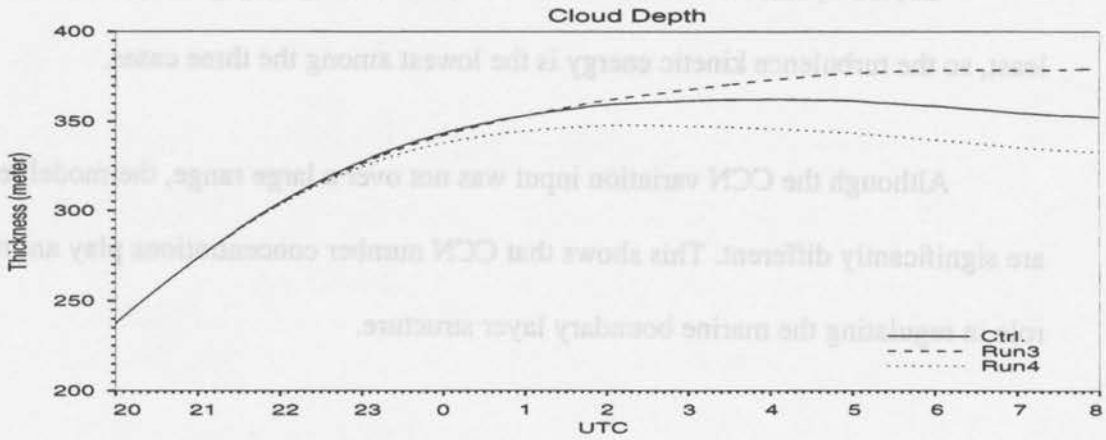

Fig. 6.6.Sensitivity tests of the varying [CCN] on cloud depth. Solid line the control run. Dashed line fixing [CCN]. Dotted line assuming $[CCN]_{top}$ = 100 cm^{-3}.

Fig. 6.7 shows the effects of varying [CCN] on the turbulence kinetic energy. In Run 3, since the cloud is the thickest, the buoyancy production contributed from the cloud layer is the largest and the boundary layer is the most turbulent (e.g., the TKE has the highest value.).

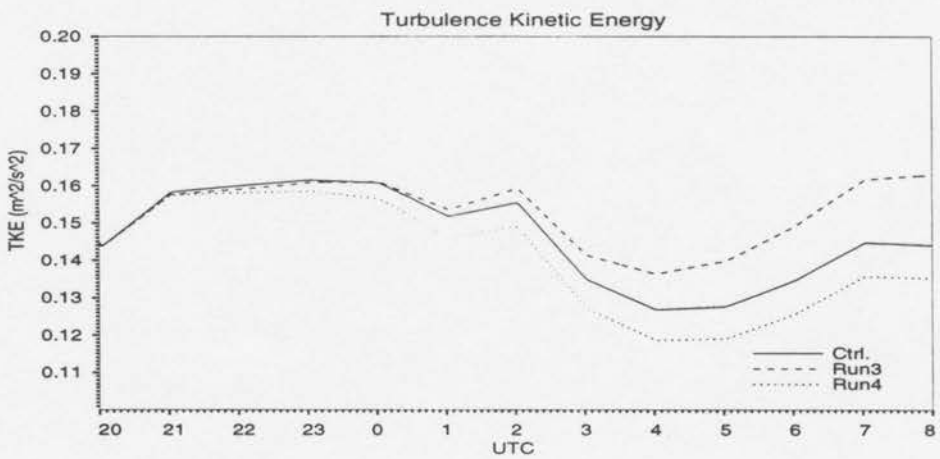

Fig. 6.7. Sensitivity tests of the varying [CCN] on the turbulence kinetic energy. Solid line the control run. Dashed line fixing [CCN]. Dotted line assuming $[CCN]_{top}$ = 100 cm^{-3}.

In Run 4, since the cloud is the thinnest, the buoyancy production of TKE is the least, so the turbulence kinetic energy is the lowest among the three cases.

Although the CCN variation input was not over a large range, the model responses are significantly different. This shows that CCN number concentrations play an important role in regulating the marine boundary layer structure.

Chapter 7

Conclusions and Future Work

7.1. Summary and Conclusions

The main goal of this report is to study the interactions between aerosols and clouds. It focuses on marine stratocumulus cloud formation and dissipation, including a parameterization of drizzle formation, which is regulated by the CCN number concentrations.

A stratocumulus-capped mixed-layer model has been developed and tested using observations from ASTEX, 1992. The hourly averaged data on SST, surface pressure (p_s), and boundary layer top conditions (r_{top}, h_{top} and v_{top}), mean winds (v_m), large-scale divergence (Div) and the radiative cooling rate (R) are prescribed from the observation. The model prognostically determines the boundary layer depth (ΔP_m), the mean total water mixing ratio (r_m), the mean moist static energy (h_m), the CCN number concentration (N_{CCN}), and the turbulence kinetic energy (e_m). The model results are in good agreement with available observations.

The drizzle parameterization is developed, based mainly on Redelsperger and Sommeria (1986)'s work, with a new drizzle autoconversion rate regulated by the total cloud droplet number concentration, which is set equal to $[N_{CCN}]$ in the cloud layer. Cloud droplet sizes are assumed to follow a gamma distribution. The coalescence threshold radius is taken as 19 μm (Fletcher, 1966; Gerber, in press). The predicted drizzle rates

are in good agreement with the ASTEX data. The highest simulated surface drizzle rate is about 1.4 mm day^{-1}, while the observed surface drizzle rate during ASTEX L1 was about 1 mm day^{-1}.

As the CCN number concentration varies, the drizzle production rate changes correspondingly. It was found that, as CCN number concentration decreases, the drizzle production rate increases and the cloud becomes thinner. These results have been obtained for an evolving marine boundary layer, without making the assumption that the cloud water content is fixed (Albrecht, 1989). At higher CCN number concentrations, the drizzle rate is suppressed and the cloud becomes thicker.

In the model, the aerosol particles are divided into two modes. The smaller mode represents the nucleation mode particles. The other represents the CCN mode particles. The study of the aerosol evolution in this report is motivated by two goals. One is to formulate CCN number and mass concentration budgets and to study the possible aerosol source and sink processes in the marine boundary layer. The second is to study the possibility of multiple steady states as mentioned by Baker and Charlson (1990). It was found in agreement with the work of B&C that there are two steady states for the CCN number concentration. One represents a normal marine air mass case with drizzle. The other resembles a continental air mass case in which coagulation, dry deposition and entrainment are dominant processes, and no precipitation occurs. In this model, the transition between the two steady states is smooth. This supports some observations that suggest there is no sharp transition between the drizzling and non-drizzling steady states of CCN number concentration in the marine boundary layer (Gerber, in press).

The results presented here help in understanding the important role of CCN in the formation and dissipation of marine boundary layer cloud. Although the mixed layer model structure is simple, the progress in simulating the drizzling boundary layer is significant.

7.2. Future work

Many cloud microphysical processes have been simplified in the present model. For example, the droplet terminal velocity, which is a function of droplet size, is assumed constant. The evaporation constant, which should be a function of temperature and saturation pressure, is assumed constant as well. The autoconversion parameterization needs to be tested further. Observations of the ratio of larger CCN number concentrations to the total CCN number concentrations in cloud would be very helpful in determining a reasonable α_{cr}. It might also be useful to try a higher-order closure model for the same case study.

Additional studies using the aerosol model should also be completed. A modeling study of the steady state CCN budget which covers a larger parameter space will improve the understanding of the CCN sources, sinks and transport. Coupling the aerosol treatment into a general circulation model would be a very interesting research topic as well.

Reference

Ackerman, Andrew S., Owen B. Toon, and Peter V. Hobbs, 1993: Dissipation of marine stratiform clouds and collapse of the marine boundary layer due to the depletion of cloud condensation nuclei by clouds. *Science*, **262**, 226-229.

Albrecht, B. A., D. A. Randall, and S. Nicholls, 1988: Observations of marine stratocumulus during FIRE. *Bull. Amer. Meteor. Soc.*, **69**, 618-626.

Albrecht, B. A.,1989: Aerosols, cloud microphysics, and fractional cloudiness. *Science* **245**, 1227-1230.

Albrecht, B. A., 1993: the effects of precipitation on the trade-wind boundary layer structure. *J. Geophys. Res.*, **98**, 7327-7337.

Baker, M. B., and R. J. Charlson, 1990: Bistability of CCN concentrations and thermodynamics in the cloud-topped boundary layer. *Nature*, **345**, 142-144.

Baker, M. B., 1993: Variability in concentrations of cloud condensation nuclei in the marine cloud-topped boundary layer. *Tellus*, **45B**, 458-472

Ball, F. K., 1960: Control of inversion height by surface heating. *Quart. J. Roy. Meteor. Soc.*, **86**, 483.

Beard., K. V., and H. T. Ochs III, 1993: Warm-rain initiation: An overview of microphysical mechanisms. *J. Appl. Meteor.*, **32**, 608-625.

Betts, A. K., and R. Boers, 1990: A cloudiness transition in a marine boundary layer. *J. Atmos. Sci.*, **47**, 1480-1497.

Bougeault, Ph., 1981: Modeling the trade-wind cumulus boundary layer. Part II: A higher-order one-dimensional model. *J. Atmos. Sci.*, **38**, 2429-2439.

Bretherton, C. S., P. Austin, and S. T. Siems, 1995: Cloudiness and marine boundary layer dynamics in the ASTEX lagrangian experiments. Part II: Cloudiness, Drizzle, Surface fluxes, and Entrainment. *J. Atmos. Sci.*, **52**, 2724-2735.

Brost, R. A., D. H. Lenschow, and J. C. Wyngaard, 1982: Marine stratocumulus layers. Part II: Turbulence budgets. *J. Atmos. Sci.*, **39**, 818-836.

Charlson, R. J., J. Langer, H. Rhode, C. B. Leovy and S. G. Warren (1991): *Tellus*, **43AB**, 152-163.

Chen, C., and W. R. Cotton, 1987: The physics of the marine stratocumulus-capped mixed layer. *J. Atmos. Sci.*, **44**, 2940-2950.

Clark, T. L., 1974: A study in cloud phase parameterization using the grama distribution. *J. Atmos. Sci.*, **31**, 142-155.

Curry, J. A., and G. F. Herman, 1985: Infrared radiative properties of summertime arctic stratus clouds. *J. Climate Appl. Meteor.*, **24**, 525-538.

Deardorff, J. W., 1974a: Three-dimensional numerical study of the height and mean structure of a heated planetary boundary layer. *Bound. Layer Meteor.*, **7**, 81-106.

Deardorff, J. W., 1974b: Three-dimensional numerical study of turbulence in an entraining mixed layer. *Bound. Layer Meteor.*, **7**, 199-266.

Deardorff, J. W., 1980a: Cloud top entrainment instability. *J. Atmos. Sci.*, **37**, 131-147.

Deardorff, J. W., 1980: Stratocumulus-capped mixed layer derived from a three-dimensional model. *Boundary Layer Meteor.*, **18**, 495-527.

Duynkerke, P. G., H. Zhang, and P. J. Jonker, 1995: Microphysical and turbulent structure of nocturnal stratocumulus as observed during ASTEX. *J. Atmos. Sci.*, **52**, 2763-2777.

Feingold, G., B. Stevens, W. R. Cotton, and A. S. Frisch, in print: On the relationship between turbulent kinetic energy and drizzle production in numerically simulated stratocumulus clouds. Submitted, *J. Atmos. Sci.*

Feingold, G., B. Stevens, W. R. Cotton and R. L. Walko, 1994: An explicit cloud microphysical/LES model designed to simulate the Twomey effect. *Atmos. Res.*, **33**, 207-233.

Fletcher, N. H., 1966: The physics of rainclouds. *Cambridge University Press, NY.* pp. 390.

Garratt, 1977: Review of drag coefficients over oceans and continents. *Mon. Wea. Rev.*, **105**, 915-929.

Gerber, H., in print: Microphysics of marine stratocumulus clouds with two drizzle modes. Submitted, *J. Atmos. Sci.*

Hartmann, D. L., M. E. Ocker-Bell, and M. L. Michelsen, 1992: The effect of cloud type on earth's energy balance: Global analysis. *J. Climate*, **5**, 1281-1304.

Kahn, P. H., and J. A. Businger, 1979: The effect of radiative flux divergence on entrainment of a saturated convective boundary layer. *Quart. J. Roy. Meteor. Soc.*, **105**, 303-306.

Kessler, E., 1969: On the distribution and continuity of water substance in atmospheric circulations. *Meteor. Monogr.*, **No. 32**, *Amer. Meteor. Soc.*, 84pp

Klein, S. A. and D. L. Hartmann, 1993: The seasonal cycle of low stratiform clouds. *J. Climate*, **6**, 1587-1606.

Kolmogorov, A. N., 1941: Energy dissipation in locally isotropic turbulence. *Doklady AN SSSR*, **32**, No. 1, 19-21.

Krasner, R. D., 1993: Further development and testing of a second-order bulk boundary layer model. *Atmospheric Science department paper,* **No. 528**, Colorado State University.

Kreidenweis, S. M. and Seinfeld, J. H., 1988: Nucleation of sulfuric-acid water and methanesulfonic acid water solution particles. Implications for the atmospheric chemistry of organosulfur species. *Atmos. Environ.*, **22**, 283-296.

Kreidenweis, S. M. and G. Feingold, 1995: Modeling of aerosol and cloud microphysical processes. *AAAR Tutorial.*

Kuo, H. C., and W. H. Schubert, 1988: Stability of cloud-topped boundary layers. *Quart. J. Roy. Meteor. Soc.*, **114**, 887-916.

Lilly, D. K., 1968: Models of cloud-topped mixed layers under a strong inversion. *Quart. J. Roy. Meteor. Soc.*, **94**, 292-309.

Lilly, D. K., and W. H. Schubert, 1980: The effects of radiative cooling in a cloud-topped mixed layer, *J. Atmos. Sci.*, **37**, 482-487.

Levin, L. M., 1958: Functions to present drop size distributions in clouds. The optical density of clouds. *Isv. Akad. Nauk SSSR, Ser. Geofiz.*, **10**, 698-702.

Moeng, C. H., and A. Arakawa, 1980: a numerical study of a marine subtropical stratus cloud layer and its stability. *J. Atmos. Sci.*, **37**, 2661-2676.

Moeng, C. H., and D. A. Randall, 1984: Problems in simulating the stratocumulus-topped mixed layer with a third-order closure model. *J. Atmos. Sci.*, **41**, 1588-1600.

Nicholls, S. H., 1984: The dynamics of stratocumulus: Aircraft observations and comparison with a mixed-layer model. *Quart. J. Roy. Meteor. Soc.*, **110**, 783-820.

Obukhov, A. M., 1941: Energy distribution in the spectrum of a turbulent flow. *Izvestiya AN SSSR, Ser. Geogr. Geofiz.*, No. 4-5, 453-466.

Oliver, D. A., W. S. Lewellen and G. G. Williamson, 1978: The interaction between turbulent and radiative transport in the development of fog and low-level stratus. *J. Atmos. Sci.*, **35**, 301-316.

Pandis, S. N., L. M. Russell, and J. H. Seinfeld, 1994: The relationship between DMS flux and CCN concentration in remote marine regions. *J. Geophy. Res.*, **99**, p. 16945+.

Pruppacher, H. R., and J. D. Klett, 1978: Microphysics of clouds and precipitation. *D. Reindel Pub., NY*, 714 pp.

Quinn, P. K., D. S. Covert, T. S. Bates, V. N. Kapustin, D. C. Ramsey-Bell, and L. M. McInnes, 1993: Dimethylsulfide cloud condensation nuclei system relevant size-resolved measurements of the chemical and physican properties of atmospheric aerosol particles, *J. Geophys. Res.*, **98**, 10411-10428.

Randall, D. A., 1980a: Conditional instability of the first kind upside-down. *J. Atmos. Sci.*, **37**, 125-130.

Randall, D. A., 1980b: Entrainment into a stratocumulus layer with distributed radiative cooling. *J. Atmos. Sci.*, **37**, 148-159.

Randall, D. A., 1984a: Buoyant production and consumption of turbulence kinetic energy in cloud-topped mixed layers. *J. Atmos. Sci.*, **41**, 402-413.

Randall, D. A., 1984b: Stratocumulus cloud deepening through entrainment. *Tellus*, **36A**, 446-457.

Randall, D. A., J. A. Coakley, Jr., C. W. Fairall, R. A. Kropfli and D. H. Lenschow, 1984: Outlook for research on subtropical marine stratiform clouds. *Bull. Amer. Meteor. Soc.*, **65**, 1290-1301.

Randall, D. A., and Q. Shao, 1992: A second-order bulk boundary-layer model. *J. Atmos. Sci.*, **49**, 1903-1923.

Redelsperger, J. L., and G. Sommeria, 1986: Three-dimensional simulation of a convective storm: Sensitivity studies on subgrid parameterization and spatial resolution. *J. Atmos. Sci.*, **43**, 2691-2635.

Schmetz, J., A. Slingo, S. Nicholls, and E. Raschke, 1983: Case studies of radiation in the cloud-capped atmospheric boundary layer. *Philos. Trans. Roy. Soc. London*, **308**, 377-388.

Seinfeld, J. H., 1986: Atmospheric chemistry and physics of air pollution. *A Wiley interscience publication, New York*. 300 pp.

Shao, Q., 1994: The effects of cloud-top processes on convection in the cloud-topped boundary layer. Department Paper, **No. 573**, Dept. of Atmos. Sci., Colorado State University.

Slingo, A., 1989: A GCM parameterization for the shortwave radiative properties of water clouds. *J. Atmos. Sci.*, **46**, 1419-1427.

Stage, S., and J. Businger, 1981: A model for entrainment into a cloud-topped marine boundary layer. Part II: Discussion of model behavior and comparison with other models. *J. Atmos. Sci.*, **38**, 2230-2242.

Stevens, B., G. Feingold, W. R. Cotton, and R. L. Walko, 1995: On elements of the micro-

physical structure of numerically simulated stratocumulus. Submitted, *J. Atmos. Sci.*

Stull, R. B., 1976: The energetics of entrainment across a density interface. *J. Atmos. Sci.*, **33**, 1260-1267.

Stull, R. B., 1988: An introduction to boundary layer meteorology. Kluwer Academic Publishers, Boston, 570 pp.

Tripoli, G. J., and W. R. Cotton, 1980: A numerical investigation of several factors contributing to the observed variable intensity of deep convection over south Florida. *J. Appl. Meteor.*, **16**, 185-220.

Twomey, S. 1977: *Atmospheric Aerosols*, **287-290** (Elsevier, amsterdam).

Twomey, S., Pipegrass, M. and wolfe, T. L., 1984: The impact of pollution on global cloud albedo. *Tellus*, **36B**, 356-366.

Young, K. C., 1993: Microphysical processes in clouds. *Oxford University Press, NY*, pp. 427.

Wakefiedl, J. S., and W. H. Schubert, 1981: Mixed-layer model simulation of eastern north pacific stratocumulus. *Mon. Wea. Rev.*, **109**, 1952-1968.

Wang, Q., and B. A. Albrecht, 1994: Observations of cloud-topped entrainment in marine stratocumulus clouds. *J. Atmos. Sci.*, **51**, 1530-1547.

Wang, S., and Q. Wang, 1994: Roles of drizzle in a one-dimensional third-order turbu-

lence closure model of the nocturnal stratus-topped marine boundary layer. *J. Atmos. Sci.*, **51**, 1559-1576.

Appendix A

Derivation of Mixed Layer Governing Equations

In this Appendix, the mixed layer mean moist static energy, total mixing ratio and boundary layer depth budget equations shown in eqns. (3.1), (3.2) and (3.3) are derived.

Reynolds averaging and assuming no external forcing, starting with the conservation law of any variable S:

$$\frac{\partial}{\partial t}(\rho\bar{S}) + \nabla\bullet(\rho\bar{\underset{\sim}{v}}\bar{S}) + \frac{\partial}{\partial z}(\rho\bar{w}\bar{S} + \rho\overline{w'S'}) = 0. \tag{A.1}$$

Using Leibniz's theorem:

$$\frac{d}{dt}\left[\int_{S_1(t)}^{S_2(t)} A(t,s)\,ds\right] = \int_{S_1(t)}^{S_2(t)} \left[\frac{\partial}{\partial t}A(t,s)\right]ds + A(t,S_2)\frac{dS_2}{dt} - A(t,S_1)\frac{dS_1}{dt}, \tag{A.2}$$

where S_1 and S_2 are the limits of integration and change with time. s is an arbitrary integration variable.

Integrating eqn. (A.1) from $Z_{S'}$ to $Z_{B'}$, where Z refers to the height in meters:

$$\frac{\partial}{\partial t}\left(\int_{z_{S'}}^{z_{B'}} (\rho\bar{S})\, dz\right) - (\rho\bar{S})_{B'}\frac{\partial z_{B'}}{\partial z} + (\rho\bar{S})_{S'}\frac{\partial z_{S'}}{\partial z} + \nabla\bullet\left(\int_{z_{S'}}^{z_{B'}} (\rho\underline{v}\bar{S})\, dz\right) -$$

$$(\rho\underline{v}\bar{S})_{B'}\nabla z_{B'} + (\rho\underline{\bar{v}}\bar{S})_{S'}\nabla z_{S'} + (\rho\overline{\bar{w}\bar{S}} + \rho\overline{w'S'})_{B'} - (\rho\overline{\bar{w}\bar{S}} + \rho\overline{w'S'})_{S'} = 0. \tag{A.3}$$

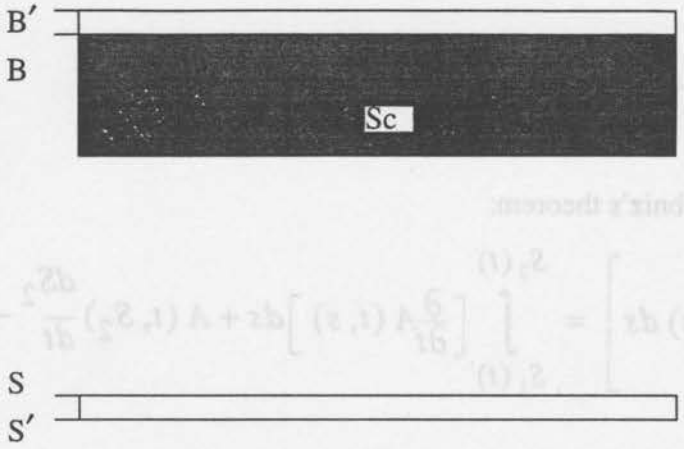

Fig. A.1 Illustration of integration domain area. B-B′ indicates the infinite thin entrainment layer. B′ refers to the interface between turbulence layer and stable free atmosphere layer. It indicates the boundary layer height. B represents the inner turbulent layer. In the same way, S′-S indicates the ultra thin surface layer. S represents the surface air inside of turbulent layer while S′ refers to the surface property.

Using the hydrostatic relation: $\rho\,(z_{B'} - z_{S'}) = \dfrac{\Delta P_m}{g}$, and defining S_m as a mean variable, one obtains the relations:

$$\int_{z_{S'}}^{z_{B'}} (\rho\bar{S})\, dz = S_m\rho\,(z_{B'} - z_{S'}) = \frac{S_m\Delta P_m}{g}, \tag{A.4}$$

and

$$\int_{z_{S'}}^{z_{B'}} (\rho \bar{\underset{\sim}{v}} \bar{S})\, dz = (\bar{\underset{\sim}{v}} \bar{S})_m \rho\, (z_{B'} - z_{S'}) \cong \bar{\underset{\sim}{v}}_m \frac{S_m \Delta P_m}{g}, \tag{A.5}$$

Defining the entrainment mass flux as (discussed in Appendix B):

$$E = \rho\, (\frac{\partial z_{B'}}{\partial t} + \bar{\underset{\sim}{v}} \cdot \nabla z_{B'} - \bar{w}_{B'})\,. \tag{A.6}$$

Assuming no cross-surface mass transport, the summation of the arrow terms in (A.3) equals zero. Rearranging (A.3), one obtains:

$$\frac{\partial}{\partial t}(S_m \Delta P_m) + \nabla \bullet (\underset{\sim}{v}_m S_m \Delta P_m) = g E S_{B'} + \rho\, (\overline{w'S'})_{S'}. \tag{A.7}$$

Remember that S_m is arbitrary; with S_m=1, the turbulent flux term in eqn. (A.7) is zero, and we get:

$$\frac{\partial}{\partial t}\Delta P_m + \nabla \bullet (\bar{\underset{\sim}{v}}_m \Delta P_m) = g E. \tag{A.8}$$

Since $\nabla \bullet (\bar{\underset{\sim}{v}}_m \Delta P_m) = \Delta P_m \cdot \nabla \bullet \bar{\underset{\sim}{v}}_m + \bar{\underset{\sim}{v}}_m \cdot \nabla\, (\Delta P_m)$, (A.9)

($\nabla(\Delta P_m) \to 0$)

eqn. (A.8) can be rewritten:

$$\frac{\partial}{\partial t}\Delta P_m = g E - (\Delta P_m \cdot \nabla \bullet \bar{\underset{\sim}{v}}_m)\,, \tag{A.10}$$

which is the equation for the boundary layer depth (3.3). This indicates that the boundary layer growth is a balance between the cloud top entrainment and large-scale divergence. Strong entrainment rate favors the PBL growth while strong divergence makes the PBL shrink.

The LHS of eqn. (A.7) may be expanded as:

$$\frac{\partial}{\partial t}(S_m \Delta P_m) + \nabla\bullet(\underset{\sim}{v}_m S_m \Delta P_m) = \Delta P_m \frac{\partial S_m}{\partial t} + S_m \frac{\partial}{\partial t}\Delta P_m$$

$$+ S_m \nabla\bullet(\underset{\sim}{v}_m \Delta P_m) + \underset{\sim}{v}_m \Delta P_m \bullet \nabla \overset{0}{\cancel{S_m}} \quad . \qquad \text{(A.11)}$$

Rearranging (A.11), substituting (A.10) and including the external forcing of precipitation. Then setting $S_m = r_m$:

$$\frac{\partial r_m}{\partial t} = \frac{g}{\Delta P_m}\left[\overline{(w'r')}_S + E\,(r_{B'} - r_m)\right] - \int_{P_{B'}}^{P_{S'}} (Auto + Evap)\, dp, \qquad \text{(A.12)}$$

which is the conservation equation for total mixing ratio eqn. (3.2). Note here, the surface flux subscript is S. In the ultra-thin surface layer, one characteristic is that the turbulent fluxes are constant with height. Therefore, the flux at level S equals that at S'.

Eqn. (A.12) shows that the surface moisture flux is the major source of PBL moisture. Dry air entrained may make the PBL drier. Precipitation depletes the water content of the PBL.

Similarly, setting $S_m = h_m$ and adding the radiation flux into the turbulence flux term, we will reach:

$$\frac{\partial h_m}{\partial t} = \frac{g}{\Delta P_m}\left[(\overline{w'h'})_S + E\,(h_{B'} - h_m) - \Delta R\right], \qquad \text{(A.13)}$$

where $\Delta R = R_{B'} - R_{S'}$, $R_{S'} = 0$.

Eqn. (A.13) is the conservation equation for moist static energy in eqn. (3.1). For the moist static energy budget in a nocturnal case, surface flux is a major supply. Entrainment might

be a production or a consumption term in the energy budget, depending on the free atmosphere conditions. Radiative cooling at the cloud top reduces the moist static energy.

Appendix B

Derivation of Entrainment Mass Flux

The entrainment mass flux, E, is derived in this appendix. The idea is to try to determine the mass flux through the infinitely thin entrainment layer, B-B', in Fig. A.1.

Start with (A.1) adding an external forcing Q_s (such as radiative forcing, solar heating, etc.):

$$\frac{\partial}{\partial t}(\rho\bar{S}) + \nabla\bullet(\rho\underset{\sim}{\bar{v}}\bar{S}) + \frac{\partial}{\partial z}(\rho\bar{w}\bar{S} + \rho\overline{w'S'}) = Q_s. \tag{B.1}$$

Integrating from z_B to $z_{B'}$, using Leibniz's theorem, one obtains:

$$\frac{\partial}{\partial t}\left(\int_{z_B}^{z_{B'}} (\rho\bar{S})\,dz\right) - \left[(\rho\bar{S})_{B'}\frac{\partial z_{B'}}{\partial t} - (\rho\bar{S})_B\frac{\partial Z_B}{\partial t}\right] + \nabla\bullet\left(\int_{z_B}^{z_{B'}} (\rho\underset{\sim}{\bar{v}}\bar{S})\,dz\right)$$

$$- [(\rho\underset{\sim}{\bar{v}}\bar{S})_{B'}\nabla z_{B'} - (\rho\underset{\sim}{\bar{v}}\bar{S})_B\nabla z_B] + [(\rho\bar{w}\bar{S})_{B'} - (\rho\bar{w}\bar{S})_B] = (\rho\overline{w'S'})_B$$

$$- (\rho\overline{w'S'})_{B'} + \int_{z_B}^{z_{B'}} Q_S dz. \tag{B.2}$$

Since $z_{B'} = z_B + \varepsilon$, the first term and the third term equal zero and $\frac{\partial z_{B'}}{\partial t} = \frac{\partial z_B}{\partial t}$. The layer above B′ is not turbulent, so the second from last term is zero. Rearranging eqn. (B.2),

$$\Delta(\rho\bar{S})\frac{\partial z_B}{\partial t} + \Delta(\rho\underset{\sim}{\bar{v}}\bar{S})\nabla z_B - \Delta(\rho\bar{w}\bar{S}) = -(\rho\overline{w'S'})_B - \int_{z_B}^{z_{B'}} Q_S dz, \tag{B.3}$$

where the Δ terms represent the differences between B and B′.

Setting $S=1$, $Q_S=0$, then $S'=0$, (B.3) is simplified to:

$$E_B = \rho_{low}\left(\frac{\partial z_B}{\partial t} + \bar{\underset{\sim}{v}}_B \nabla z_B - \bar{w}_B\right) = \rho_{up}\left(\frac{\partial z_{B'}}{\partial t} + \bar{\underset{\sim}{v}}_{B'} \nabla z_{B'} - \bar{w}_{B'}\right) = E_{B'}.$$

(B.4)

Defining $E=E_B=E_{B'}$, and substituting (B.4) into (B.3),

$$\left(\rho\overline{w'S'}\right)_B = -E\Delta\bar{S} + \int_{z_B}^{z_{B'}} Q_S dz, \tag{B.5}$$

which is the boundary layer top flux formula.

If $\bar{S} = \bar{r}_m$ is assumed, $Q_S = 0$, and the moisture flux is obtained:

$$\left(F_r\right)_B = \left(\rho\overline{w'S'}\right)_B = -E\Delta\bar{S}. \tag{B.6}$$

If $\bar{S} = \bar{h}_m$ is assumed, $Q_S = \frac{\partial R}{\partial z}$, and the moist static energy flux is obtained:

$$\left(F_h\right)_B = \left(\rho\overline{w'h'}\right)_B = -E\Delta\bar{h} + \Delta R. \tag{B.7}$$

Therefore, the moisture and moist static energy fluxes have been connected with the entrainment process and the free atmosphere air conditions. Strong entrainment will lead to strong turbulence fluxes at the cloud top.